Membrane binding properties of the cytoskeletal protein bactofilin

Ying Liu[1,#], Rajani Karmakar[2], Maria Billini[1], Wieland Steinchen[3,4], Saumyak Mukherjee[2,$], Rogelio Hernández-Tamayo[5,6], Thomas Heimerl[4], Gert Bange[3,4,7], Lars V. Schäfer[2], Martin Thanbichler[1,4,7*]

[1] Department of Biology, Marburg University, 35032 Marburg, Germany
[2] Theoretical Chemistry, Ruhr University Bochum, 44780 Bochum, Germany
[3] Department of Chemistry, Marburg University, 35032 Marburg, Germany
[4] Center for Synthetic Microbiology (SYNMIKRO), 35032 Marburg, Germany
[5] Microcosm Earth Center, 35032 Marburg, Germany
[6] Max Planck Fellow Group Bacterial Cell Biology, Max Planck Institute for Terrestrial Microbiology, 35043 Marburg, Germany
[7] Max Planck Fellow Group Molecular Physiology of Microbes, Max Planck Institute for Terrestrial Microbiology, 35043 Marburg, Germany

[#] Present address: Universitätsklinikum Schleswig-Holstein, 24105 Kiel, Germany
[$] Present address: Department of Theoretical Biophysics, Max Planck Institute of Biophysics, 60438 Frankfurt am Main, Germany

*Address correspondence to
Martin Thanbichler (thanbichler@uni-marburg.de)

Keywords
Cytoskeletal protein, bactofilin, CcmA, membrane-targeting sequence, membrane binding

Abstract

Bactofilins are a widespread family of cytoskeletal proteins with important roles in bacterial morphogenesis, chromosome organization and motility. They polymerize in a nucleotide-independent manner, forming non-polar filaments that are typically associated with the cytoplasmic membrane. Membrane binding was suggested to be mediated by a short N-terminal peptide, but the underlying mechanism and the conservation of this interaction determinant among bacteria remain unclear. Here, we use the bactofilin homolog BacA of the stalked bacterium *Caulobacter crescentus* as a model to analyze the membrane-binding behavior of bactofilins. Based on site-directed mutagenesis of the N-terminal region, we identify the full membrane-targeting sequence of BacA (MFSKQAKS) and pinpoint amino acid residues that are critical for its function *in vivo* and *in vitro*. Molecular dynamics simulations then provide detailed insight into the molecular mechanism underlying the membrane affinity of this peptide. Collectively, these analyses reveal a delicate interplay between the water exclusion of hydrophobic N-terminal residues, the arrangement of the peptide within the membrane and the electrostatic attraction between positively charged groups in the peptide and negative charges in the phospholipid molecules. A comprehensive bioinformatic analysis shows that the composition and properties of the membrane-targeting sequence of BacA are conserved in numerous bactofilin homologs from diverse bacterial phyla. Importantly, our findings reveal cooperative effects between the membrane-binding and polymerization activities of BacA. Moreover, they demonstrate that both of these activities critically contribute to the recruitment of the BacA client protein PbpC, a membrane-bound cell wall synthase that uses a conserved peptide in its N-terminal cytoplasmic tail to interact with BacA assemblies. Finally, we show that PbpC can functionally replace the endogenous membrane-targeting sequence of BacA when provided at elevated levels *in trans*, indicating that client proteins can make a significant contribution to the membrane association of bactofilin polymers. Together, these results unravel the mechanistic underpinnings of membrane binding by bactofilin homologs, thereby illuminating a previously obscure but important aspect in the biology of this cytoskeletal protein family.

Introduction

Cytoskeletal proteins mediate a variety of fundamental cellular processes in bacteria, including cell growth, cell division and DNA segregation (Cabeen and Jacobs-Wagner, 2010; Wagstaff and Löwe, 2018). Many important components of the bacterial cytoskeleton have eukaryotic homologs. The conserved cell division protein FtsZ, for instance, is a member of the tubulin superfamily (Löwe and Amos, 1998; Mukherjee et al., 1993), forming dynamic polymers at the cell division site that control the assembly and function of the cell division apparatus (McQuillen and Xiao, 2020). By contrast, the morphogenetic protein MreB, which governs cell growth and morphology in most rod-shaped bacteria (Jones et al., 2001; van den Ent et al., 2001), is homologous to actin (Rohs and Bernhardt, 2021). Some bacteria also possess intermediate-filament-like proteins, such as the coiled-coil-rich protein crescentin, which promotes cell curvature in the crescent-shaped alphaproteobacterium *Caulobacter crescentus* (Ausmees et al., 2003; Liu et al., 2024). Apart from these universally conserved cytoskeletal protein families, bacterial cells can contain various polymer-forming proteins that are typically absent from eukaryotes (Wagstaff and Löwe, 2018). A prominent member of this group of proteins is bactofilin (Kühn et al., 2010).

Bactofilin homologs are widespread among bacteria and involved in diverse cellular functions. In many species, they have important roles in cell shape determination, including the establishment or adjustment of cell curvature in *Helicobacter pylori* (Sycuro et al., 2010), *Campylobacter jejuni* (Frirdich et al., 2023), *Leptospira biplexa* (Jackson et al., 2018) and *Rhodospirillum rubrum* (Pöhl et al., 2024), the modulation of cell size in *Chlamydia trachomatis* (Brockett et al., 2021), the formation of buds in *Hyphomonas neptunium* (Pöhl et al., 2024), the stabilization of rod shape in *Myxococcus xanthus* (Koch et al., 2011) and *Proteus mirabilis* (Hay et al., 1999) and the synthesis of stalk-like cellular extensions in *C. crescentus* (Kühn et al., 2010), *Asticcacaulis biprosthecum* (Caccamo et al., 2020) and *Rhodomicrobium vannielii* (Richter et al., 2023). Other functions include DNA organization in *M. xanthus* (Anand et al., 2020; Lin et al., 2017) as well as cell motility in *Bacillus subtilis* (El Andari et al., 2015). Bactofilins are relatively small proteins characterized by a central Bactofilin A/B domain (InterPro ID: IPR007607) that is typically flanked by unstructured terminal regions of varying lengths. The central domain is ~110 amino acids long and folds into a compact right-handed β-helix with a triangular geometry, measuring roughly 3 nm along its longitudinal axis (Kassem et al., 2016; Shi et al., 2015; Vasa et al., 2015; Zuckerman et al., 2015). This basic unit polymerizes into extended non-polar filaments through alternating head-to-head and tail-to-tail interactions between individual subunits (Deng et al., 2019). The resulting protofilaments can further assemble into higher-order structures such as bundles, lattices and 2D crystalline sheets *in vitro* (Holtrup et al., 2019; Kühn et

al., 2010; Pöhl et al., 2024; Sichel et al., 2022; Vasa et al., 2015; Zuckerman et al., 2015) and, potentially, also *in vivo* (Kühn et al., 2010). Previous studies have indicated that bactofilins are typically associated with the cytoplasmic membrane (Deng et al., 2019; Hay et al., 1999; Koch et al., 2011; Kühn et al., 2010; Lee et al., 2023). However, only a small subset of them, including certain gammaproteobacterial representatives (Hay et al., 1999), contain predicted transmembrane helices, suggesting that canonical bactofilins use an unconventional membrane-targeting mechanism that may have specifically evolved in this cytoskeletal protein family. Consistent with this notion, the membrane-binding activity of bactofilin homologs from *Thermus thermophilus* (Deng et al., 2019) and *C. trachomatis* (Lee et al., 2023) has recently been shown to depend on a short peptide in the N-terminal unstructured region of the proteins. However, the conservation of this peptide, the precise mechanism underlying its affinity for the lipid bilayer, and the interplay between membrane attachment and bactofilin polymerization still remain to be investigated.

In this study, we comprehensively analyze the membrane-binding behavior of bactofilins, using BacA from *C. crescentus* as a model protein. Previous work has shown that BacA forms membrane-associated polymeric sheets at the old pole of the *C. crescentus* cell, which recruit the cell wall synthase PbpC to stimulate stalk formation at this subcellular location (Billini et al., 2019; Hughes et al., 2013; Kühn et al., 2010). By systematically exchanging residues in the N-terminal region of BacA, we identify a short N-terminal peptide (MFSKQAKS) that acts as the membrane-targeting sequence (MTS) of BacA and pinpoint residues critical for its membrane-binding activity *in vivo* and *in vitro*. We then clarify the molecular mechanism underlying the membrane affinity of this sequence using molecular dynamics simulations. A comprehensive bioinformatic analysis suggests that the mode of action identified for the MTS of BacA may be broadly conserved among bactofilins from various different phyla. Importantly, our findings indicate that membrane association and polymerization are cooperative processes that are both required for robust BacA assembly, with polymerization in turn promoting the interaction of BacA with its client protein PbpC, and vice versa. Together, these findings reveal the mechanistic basis of membrane binding by bactofilin homologs and highlight the implications of this process for bactofilin function, thereby shedding light on a thus-far poorly understood aspect in the biology of this widespread cytoskeletal protein.

Results

The membrane-binding activity of BacA depends on an N-terminal amphipathic peptide

Previous work has proposed a small N-terminal peptide as the membrane-targeting sequence (MTS) of canonical bactofilin homologs (Deng et al., 2019). In the case of *C. crescentus* BacA, the suggested region comprises the sequence MFSKQAKS at the N-terminal end of the protein (**Figure 1A**). To verify the importance of this peptide for BacA function, we compared the localization pattern of wild-type BacA with that of a mutant derivative lacking the predicted membrane-targeting sequence (MTS). For this purpose, the two proteins were fused to the monomeric yellow fluorescent protein mVenus and produced in a strain carrying an in-frame deletion in the endogenous *bacA* and *bacB* genes (**Figure 1B**). As expected, the wild-type protein was fully functional and formed distinct fluorescent foci at the stalked pole of the cells, which have been previously shown to reflect the formation of small patches of membrane-associated BacA polymers (Kühn et al., 2010). The mutant protein (Δ2-8), by contrast, was evenly distributed in the cytoplasm, supporting the idea that the N-terminal region of BacA is involved in membrane binding. The diffuse localization also suggests a defect in polymerization, which however may be a secondary effect resulting from the loss of membrane association, since previous work has shown that the unstructured terminal regions are not essential for bactofilin assembly (Sichel et al., 2022; Vasa et al., 2015). In line with this finding, transmission electron microscopy (TEM) analysis confirmed that the Δ2-8 variant formed polymers similar to those of wild-type BacA when overproduced in *Escherichia coli* (**Figure 1–figure supplement 1**). Thus, although not essential, membrane binding may facilitate BacA polymerization at native expression levels by promoting its enrichment at the membrane surface and thereby stimulating inter-subunit interactions. To further evaluate the role of polymerization in BacA localization, we generated a mutant variant of BacA impaired in self-assembly by replacing a conserved phenylalanine residue in the C-terminal polymerization interface of its Bactofilin A/B domain (F130 in *C. crescentus* BacA) with a charged arginine residue. Consistent with previous work in other species (Deng et al., 2019; Jacq et al., 2024; Zuckerman et al., 2015), TEM analysis (**Figure 1–figure supplement 1**) and size-exclusion chromatography studies (**Figure 1–figure supplement 2**) verified that the mutant protein (F130R) failed to form polymeric structures *in vitro*. Importantly, the corresponding mVenus fusion protein no longer formed membrane-associated polar foci but was dispersed within the cytoplasm (**Figure 1B**), suggesting that polymerization and membrane binding could stimulate each other.

Apart from transmembrane segments, proteins commonly employ amphiphilic helices to associate with the inner face of the cytoplasmic membrane, as exemplified by the bacterial actin homologs FtsA (Pichoff

and Lutkenhaus, 2005) and MreB (Salje et al., 2011). As a first step to clarify the mechanism underlying the membrane-binding activity of the MTS, we therefore determined whether it was able to adopt an amphiphilic helical structure. However, neither machine-learning-based pattern recognition, as employed by AmphipaSeeK (Sapay et al., 2006) (**Figure 1A**), nor helical wheel analysis (**Figure 1C**) provided any support for this possibility, suggesting a different mode of action.

To obtain more insight into the function of the MTS, we systematically exchanged single or multiple amino acid residues in the N-terminal eight amino acids of BacA-mVenus (**Figure 1–figure supplement 3**) and analyzed the localization patterns of the mutant proteins. Among the single exchanges, substitution of the hydrophobic phenylalanine residue at position 2 (F2Y and F2E) led to a disperse or, occasionally, patchy distribution of the fusion protein (**Figure 1B**). Other single substitutions, by contrast, had relatively mild effects, including the formation of multiple and/or mispositioned bactofilin complexes (**Figure 1–figure supplement 4**). Notably, however, a double exchange replacing the two positively charged lysine residues in the MTS with polar serine residues (K4S-K7S) strongly increased the fraction of delocalized protein (**Figure 1B**), although distinct fluorescent foci or patches were still detectable, suggesting residual membrane-binding activity. An even stronger effect, as reflected by a complete dispersion of the fluorescence signal, was observed when negatively charged glutamate residues were introduced at these positions (K4E-K7E). Collectively, these results point to a central role of F2 and K4/K7 in the association of BacA with the cytoplasmic membrane.

To further characterize the mutant BacA-mVenus variants, we analyzed their mobility within the cell using single-particle tracking (**Figure 2–video 1** and **Figure 2–figure supplement 1**). As expected, given its ability to interact with the membrane and polymerize, the wild-type protein exhibited a very low diffusional mobility. Mutant variants that were partially delocalized (F2Y and K4S-K7S) were significantly more mobile, and variants with a largely diffuse localization (Δ2-8, F2E, K4E-K7E and F2E-K4E-K7E) displayed the highest diffusion rates, approaching the mobility of free mVenus (**Figure 2A** and **Supplementary file 1**). These results support the notion that the MTS is required for the formation of stable membrane-associated BacA assemblies.

As a direct means to analyze the membrane-binding activity of the fusion proteins, we next performed cell fractionation studies. To this end, cells producing different BacA-mVenus variants were lysed and membranes were separated from soluble components by ultracentrifugation. Western blot analysis revealed that a large part of the wild-type protein was detected in the membrane fraction, whereas the variant lacking the MTS (Δ2-8) was completely soluble (**Figure 2B**). A severe reduction in membrane-

binding activity was also observed for all fusion proteins lacking residues F2 and K4/K7 (**Figure 2C**), confirming the importance of these residues in the function of the MTS.

After having identified a role of the MTS in the association of BacA with membranes *in vivo*, we aimed to verify the membrane-targeting activity of this peptide in a defined system *in vitro*. For this purpose, we purified wild-type BacA and various mutant derivatives, using a cleavable N-terminal His_6-SUMO affinity tag (Marblestone et al., 2006), which allowed us to obtain proteins without any non-native extensions that could potentially interfere with the analysis. This approach also made it possible to obtain two additional BacA variants, one lacking the N-terminal methionine of BacA (ΔM) and another one lacking the N-terminal methionine and containing a glutamate instead of the phenylalanine normally located at the second position of the MTS (xE). We then incubated the different proteins with small unilamellar vesicles (liposomes) made of phosphatidylglycerol, which has been identified as the most abundant membrane lipid in *C. crescentus* under standard growth conditions (Contreras et al., 1978; Stankeviciute et al., 2019). Subsequently, the liposomes were collected by ultracentrifugation and analyzed for the amount of bound protein (**Figure 3**). Consistent with the *in vivo* data, a large proportion (~80%) of the wild-type protein was associated with the liposome pellet, whereas only a small fraction sedimented in control reactions lacking liposomes, likely reflecting large, poorly soluble polymer bundles. Variants lacking the entire MTS (Δ2-8) or carrying the F2E or K4E/K7E exchanges, by contrast, showed severe defects in membrane binding, with sedimentation efficiencies similar to those obtained in the liposome-free control reactions. Residual binding was still observed for the F2Y and K4S/K7S variants, consistent with the milder defects observed for these proteins in the localization and single-particle tracking studies (compare **Figures 1B** and **2A**). Notably, while the behavior of the xE variant closely resembled that of the F2E variant, the absence of residue M1 (ΔM) alone only partially abolished the membrane association of BacA, indicating that the N-terminal methionine plays an important but not decisive role in the function of the MTS (**Figure 3**). Together, these findings verify the existence of an N-terminal MTS in BacA. Moreover, they identify the hydrophobic residues M1 and F2 and the two positively charged lysine residues K4 and K7 as key determinants of its membrane-binding affinity.

BacA polymerization and membrane binding are mutually stimulating processes

Our results showed that the disruption of the polymerization interface (F130R) resulted in a diffuse, cytoplasmic localization of BacA, suggesting that polymerization might be a prerequisite for efficient membrane binding (**Figure 1B**). To investigate this possibility, we clarified the membrane-binding activity of the polymerization-deficient F130R variant of BacA-mVenus. Cell fractionation experiments showed that the

fusion protein was barely detectable in the membrane fraction (**Figure 4A**). In line with this finding, only marginal membrane-binding activity was observed for the untagged BacA-F130 variant in liposome-binding assays (**Figure 4B**). These results suggest that the MTS has a relatively low affinity for the membrane, so that a stable interaction can only be achieved by cooperative binding of multiple MTS-containing N-terminal tails, arrayed on the surface of bactofilin polymers. Further support for this idea came from domain swapping experiments that showed that the MTS of BacA was able to mediate stable membrane attachment when fused to a derivative of the polymer-forming protein crescentin from *C. crescentus* lacking its native membrane-targeting sequence (**Figure 4–figure supplement 1**).

Interestingly, the diffuse localization and high diffusional mobility of BacA variants containing a defective MTS (**Figures 1B and 2A**) indicate that there may also be a converse stimulatory effect of membrane binding on BacA polymerization. To further assess this possibility, we analyzed whether an MTS-defective BacA variant could regain the ability to form membrane-associated polymeric complexes if equipped with a heterologous membrane-targeting sequence. To this end, two copies of the N-terminal amphiphilic helix of *E. coli* MreB (Salje et al., 2011) were fused to a BacA-mVenus variant lacking the native MTS-containing peptide (Δ2-8). Microscopic analysis revealed that the fusion protein condensed into distinct foci at the old pole or the cell center (**Figure 4C**), reminiscent of the aberrant localization patterns observed for mutant proteins with exchanges in the MTS that did not completely abolish membrane binding (compare **Figure 1–figure supplement 4**). The restoration of fluorescent foci was accompanied by a strong decrease in diffusional mobility, as determined by single-molecule tracking (**Figure 4D**). In addition, cell fractionation experiments showed that the fusion protein was highly enriched in the membrane pellet (**Figure 4E**). Importantly, when its polymerization interface was disrupted by introduction of the F130R exchange, focus formation was abolished, membrane binding was strongly reduced, and the diffusional mobility of the fusion protein increased to a value similar to that of an F130R variant containing the native MTS of BacA (**Figure 4C-E**). Collectively, these findings demonstrate that the polymerization and membrane-binding activities of BacA strongly stimulate each other.

Molecular dynamics simulations identify M1, K4 and K7 as key residues of the BacA MTS

To investigate the molecular underpinnings of the interaction between the MTS of BacA and the membrane, we turned to all-atom molecular dynamics (MD) simulations. For this purpose, peptides comprising the ten N-terminal bactofilin residues were simulated in the presence of a multi-component lipid bilayer that was composed of approximately 50% monoglucosyldiglyceride (GLY), 33% phosphatidylglycerol (PG) and 16% diacylglycerol (DAG) lipids (see **Supplementary file 2** for details), approximating the native com-

position of *C. crescentus* cell membranes under standard growth conditions (Chow and Schmidt, 1974; Contreras et al., 1978; Stankeviciute et al., 2019). In addition to the wild-type peptide MFSKQAKSNN, our analysis also included the mutant F2Y and K4S-K7S variants (each in a separate simulation).

The starting structures of the peptides were modeled in an extended conformation without any secondary structure. At the beginning, a single peptide (wild-type, F2Y or K4S-K7S) was placed in the aqueous phase at a distance of approximately 3 nm from the lipid headgroups. During the 500-ns simulations, all three peptides rapidly bound to the membrane and established multiple contacts with the lipids at the membrane/water interface (illustrated for the wild-type MTS in **Figure 5A**). In doing so, the peptides did not adopt any persistent secondary structures but remained disordered, with a preference for somewhat extended conformations (**Figure 5B,C** and **Supplementary file 3**). Notably, in control simulations in which the peptides were initially modeled as α-helices, the peptides unfolded rapidly, either in the aqueous phase or after binding to the membrane/water interface, eventually yielding the same results (within the statistical uncertainties) as the simulations starting from an extended conformation.

Excluding the initial phase of the simulations in which the peptides were not yet bound to the membrane, we then determined the density profiles of the three different peptides along the membrane normal (**Figure 5D** and **Figure 5–figure supplement 1**). The results show that the N-terminal residues 1 and 2 insert deeply into the lipid bilayer, assuming positions below the phosphate headgroup region, while the positions of the remaining residues (3 to 10) are gradually shifted towards the aqueous phase. The peptides thus bind to the membrane in a tilted orientation, with their N-terminal region protruding more deeply into the hydrophobic parts of the lipid headgroup region (**Figure 5B**). Interestingly, in case of the F2Y variant, the presence of tyrosine at position 2 pulls residue M1 and Y2 further towards the headgroup/water interface (**Figure 5–figure supplement 1B**). This result can be explained by the preferential hydration of tyrosine compared to phenylalanine, as is also reflected in the difference of the solvation free energies (ΔG_{solv}) of the corresponding side-chain analogs *p*-cresol (-25.6 kJ mol^{-1}) and toluene (-3.2 kJ mol^{-1}) (Wolfenden et al., 1981).

To characterize the interactions between the peptides and the membrane in more detail, the contacts between the individual peptide residues and the different lipid species in the bilayers were counted. The results confirm the above finding that residues 1 and 2 show the strongest association with lipids and that lipid interactions gradually decrease for residues further down the peptide chain (**Figure 6A**). Notably, among these interactions, contacts with anionic PG lipids dominate, even though the percentage of PG lipids (33%) in the simulated bilayer is smaller than that of GLY lipids (50%) (see above and **Supplementary**

file 2), which can largely be attributed to the lysine residues at positions 4 and 7. In line with this result, the K4S-K7S variant shows a strong reduction in the number of PG contacts at these positions, which is partially compensated by a higher prevalence of GLY contacts, particularly for residues 1 to 5 (**Figure 6A**). The F2Y variant, by contrast, did not show a marked decrease in the number of total lipid contacts for position 2, with fewer PG contacts (of residues 1 and 2) again compensated by more GLY lipid contacts (**Figure 6A**). Taken together, the lipid contact analysis shows that the N-terminal residues M1 and F2 establish the closest contacts with the lipid bilayer, and that the lysine residues K4 and K7 strongly interact with PG lipids.

The contact analysis described above only provides insight into the spatial proximity of the peptides and the lipids. To additionally determine the strength of the interactions, we analyzed the MD simulations in terms of the interaction energies between the different peptide residues and the lipid molecules (**Figure 6B**). For both the wild-type peptide and its F2Y variant, the strongest (most favorable) peptide-lipid interaction energy is seen for residues 1, 4 and 7, which can be attributed to strong electrostatic attraction between the PG lipids and the charged NH_3^+ group at the N-terminus (residue M1) as well as the side chains of residues K4 and K7, respectively. Notably, out of all residues, M1 interacts most strongly with the membrane. Nevertheless, its removal (ΔM) had only a moderate effect on the membrane-binding activity of BacA *in vitro* (**Figure 3**), corroborating the notion that the largest part of the interaction energy is provided by the N-terminal NH_3^+ group of M1 rather than its hydrophobic side chain. However, taken together, the two lysines K4 and K7 make an even larger contribution to the interaction, consistent with the significant reduction in membrane association observed for the K4S-K7S variants of BacA (**Figures 1C, 2C and 3**). It is interesting to note that in terms of the interaction energy, residue F2 does not seem to play a prominent role in the peptide-membrane association (**Figure 6B**), although the F2Y exchange strongly reduces the membrane-binding affinity of BacA (**Figures 1C, 2C and 3**). The deleterious effect of this exchange may be explained by the preferential hydration of tyrosine compared to phenylalanine, which is not reflected in the peptide-membrane interaction energy but in the difference in hydration free-energy (see above). Furthermore, residues M1 and Y2 in the F2Y peptide are located in closer proximity to the aqueous phase (see **Figure 5–figure supplement 1B**), which leads to a substantial decrease in the favorable interaction energy of the N-terminal NH_3^+-group with PG lipids that is only incompletely compensated by slightly more favorable interactions with GLY lipids (**Figure 6B**). Together, these results provide a rational basis for the experimental finding that the F2Y and K4S-K7S variants of BacA have a considerably lower membrane-binding affinity than the wild-type protein.

The N-terminal membrane-targeting sequence is conserved among bactofilin homologs

The results of the MD simulations confirmed that the short peptide (MFSKQAKS) at the N-terminus of BacA acts as an MTS. To assess whether this mode of interaction was more widespread among bactofilins, we set up a bioinformatic pipeline to analyze the conservation of the N-terminal region of bactofilin homologs from a broad range of bacterial lineages (**Figure 7–figure supplement 1**). To this end, all proteins containing an annotated bactofilin domain were retrieved from the UniProt database (UniProt Consortium, 2023). After the exclusion of entries from non-bacterial origin, we eliminated all bactofilin homologs containing predicted N-terminal transmembrane helices as a membrane anchor. These proteins were relatively rare (~3.2%) but widely distributed across the bacterial phylogeny, with the majority found in the gammaproteobacteria (**Figure 7–figure supplement 1**). To avoid biases arising from the over-representation of certain bacterial species in UniProt, we next grouped highly similar (>90% identity) bactofilin sequences, which typically represent orthologs from different sequenced strains, and only kept one sequence per group. For each of the remaining proteins, we then determined the N-terminal region preceding the bactofilin domain. Based on the length of the MTS identified for BacA, we eliminated proteins whose predicted N-terminal tails were shorter than eight amino acids, potentially due to misannotation of the translational start sites. The remaining proteins (14337 sequences) were then used to search for conserved N-terminal amino acid motifs.

A global analysis of the entire protein set yielded a conserved motif with the consensus sequence MFSKKKK, which resembled the MTS identified for *C. crescentus* BacA and contained both the two hydrophobic N-terminal residues that insert into the core of the lipid bilayer as well as the two lysin residues that make electrostatic interactions with the headgroups of PG lipids (**Figure 7**). This result suggests that the presence of an N-terminal MTS is a common feature of bacterial bactofilin homologs. However, this global approach might obscure lineage-specific adaptations of the MTS to evolutionary differences in membrane lipid composition. To address this issue, we conducted an additional analysis in which we sorted the proteins according to their phylogenetic origin before performing a motif search. In doing so, we focused on the phyla Pseudomonadota, Bacteroidota, Bacillota, Spirochaetota and Thermodesulfobacteriota, which contribute the majority of the bactofilin homologs in the UniProt database. This refined analysis confirmed the presence of conserved N-terminal motifs in each of the five phyla, although there is variability in the consensus sequences of these motifs both within and between phyla (**Figure 7–figure supplement 1**). A comparison of the most prevalent motifs (**Figure 7**) revealed that bactofilin homologs from Pseudomonadota and Bacillota share highly similar N-terminal sequences, which largely correspond to the global motif described above. A similar N-terminal motif is also found in most bactofilin homologs

from Bacteroidota, although these proteins often display a negatively rather than a positively charged residue at position 4. The most prevalent motif identified in Spirochaetota and Thermodesulfobacteriota, by contrast, is fundamentally different from the global consensus motif and may thus have a function unrelated to membrane binding (**Figure 7**). However, there is also a subset of sequences from these phyla that do share MTS-like sequences (**Figure 7–figure supplement 2**), suggesting that the ability of bactofilins to interact with membranes is still widespread in these phyla. Together, these results strongly suggest that the majority of bactofilin homologs known to date feature an N-terminal MTS whose composition and mode of action are similar to that of *C. crescentus* BacA.

BacA polymerization promotes client-protein binding

The only client protein of BacA reported to date is the cell wall synthase PbpC, a bitopic membrane protein related to *E. coli* PBP1A (Yakhnina et al., 2013; Strobel et al., 2014). Previous work has shown that its N-terminal cytoplasmic tail was sufficient for its bactofilin-dependent recruitment to the stalked cell pole of *C. crescentus*, suggesting that this region of the protein contains all critical interaction determinants (Hughes et al., 2013; Kühn et al., 2010). However, its precise mode of interaction with the polar bactofilin cluster and the role of this interaction in bactofilin assembly has remained unclear.

To clarify which of the two bactofilin paralogs of *C. crescentus* interacts with PbpC to mediate its polar localization, we analyzed the subcellular distribution of an mVenus-tagged PbpC variant in different bactofilin mutants. The fusion protein retained its wild-type localization pattern in the Δ*bacB* background but failed to condense into polar foci in Δ*bacA* cells, identifying BacA as its main interactor (**Figure 8** and **Figure 8–figure supplement 1A**). Next, we aimed to pinpoint the regions in the cytoplasmic tail of PbpC that mediate its recruitment to BacA. For this purpose, we retrieved the amino acid sequences of PbpC homologs and aligned their predicted cytoplasmic tails (**Figure 8–figure supplement 2**). This analysis identified four distinct segments, including (i) a highly conserved peptide at the N-terminal end of PbpC (region C1), (ii) a proline-rich medial region, (iii) a second highly conserved peptide (Region C2) and (iv) a region rich in positively charged amino acids immediately adjacent to the transmembrane helix. To assess the importance of these segments, we generated mVenus-PbpC derivatives whose cytoplasmic tail either lacked region C1 (Δ2-13) or only comprised region C1, with the remaining parts being replaced by an unstructured region taken from the periplasmic protein DipM of *C. crescentus* (Izquierdo-Martinez et al., 2023) (**Figure 8–figure supplement 3**). Microscopic analysis showed that the removal of region C1 resulted in the loss of polar localization, whereas the chimeric variant showed the same localization pattern as the wild-type fusion protein (**Figure 8A**). Similar results were obtained for cells that were cultivated under phosphate-

limiting condition to stimulate stalk growth (Schmidt, 1968). Interestingly, the delocalization of mVenus-PbpC upon deletion of region C1 did not reduce its ability to promote stalk elongation (**Figure 8–figure supplement 4**). Region C1 thus appears to be necessary and sufficient for the recruitment of PbpC to the cell pole-associated BacA assembly, but dispensable for its role in stalk biogenesis.

To verify the ability of region C1 to directly associate with BacA, we generated a synthetic peptide comprising the N-terminal 13 residues of PbpC and analyzed its interaction with purified BacA polymers using biolayer interferometry. When biosensors carrying the immobilized peptide were titrated with increasing concentrations of BacA, we observed specific binding with an apparent equilibrium dissociation constant (K_D) of 4.9 µM (**Figure 8B** and **Figure 8–figure supplement 5**). A similar assay with the polymerization-deficient F130R variant, by contrast, only yielded residual binding with very fast dissociation rates (**Figure 8C**). These results confirm the direct interaction of BacA with region C1 of PbpC. Moreover, they indicate that BacA polymerization is a prerequisite for efficient and stable PbpC binding, likely because the high local accumulation of BacA within polymers leads to an increase in the avidity for its interaction partner.

Having identified a direct association of BacA with the N-terminal peptide of PbpC, we set out to map the PbpC-binding site of BacA using hydrogen-deuterium-exchange (HDX) mass spectrometry, a method that allows the detection of local shifts in the accessibility of backbone amide hydrogens induced by conformational changes and/or ligand binding (Konermann et al., 2011). When analyzed alone, the HDX profile of BacA showed very fast HDX in the N- and C-terminal regions flanking the bactofilin domain, which indicates a high degree of disorder and thus corroborates the predicted domain structure of BacA (**Figure 8–figure supplement 6**). Upon incubation with the PbpC peptide, several peptides in the C-terminal half of the central bactofilin domain exhibited a small, yet significant decrease in the HDX rate (**Figure 8C**), with the most prominent changes observed in a region close to the C-terminal polymerization interface (**Figure 8D**). Although additional studies are required to precisely define the interface, this finding suggest that inter-subunit interactions in the bactofilin polymer could potentially induce slight conformational changes in BacA that promote PbpC binding.

To clarify whether the interaction with PbpC contributes to BacA assembly, we compared the localization patterns of BacA-Venus in wild-type and Δ*pbpC* cells. The behavior of the fusion protein was unchanged in the mutant background, suggesting that PbpC does not have a major role in BacA polymerization or membrane binding (**Figure 8–figure supplement 1B**). Nevertheless, it was conceivable that PbpC binding could contribute, at least to some extent, to the association of BacA polymers with the cytoplasmic mem-

brane, thereby complementing the activity of the MTS. To test this hypothesis, we set out to investigate the effect of PbpC on the assembly of an MTS-free BacA-mVenus variant (Δ2-8). Our initial studies showed that the mutant protein had a diffuse localization when analyzed in cells producing PbpC at native levels (**Figure 1B**). However, it was possible that, in this setting, the affinity between the two proteins or the number of PbpC molecules available for the interaction are not be high enough to compensate for the loss of the endogenous membrane-targeting sequence. We therefore performed localization studies in cells that overproduced a C-terminally truncated variant of PbpC in which the periplasmic region was replaced by the fluorescent protein mCherry ($PbpC_{1-132}$-mCherry) (Kühn et al., 2010), thereby accumulating elevated levels of the PbpC membrane anchor. Control experiments showed that the truncated protein colocalized with wild-type BacA-mVenus and stabilized the polar bactofilin cluster under conditions of BacA-mVenus overproduction (**Figure 9 and Figure 9–figure supplement 1**). Importantly, the increased availability of the PbpC membrane anchor also fully restored polar localization for the MTS-free fusion protein (Δ2-8), whereas it could not reverse the localization defect of the polymerization-deficient F130R variant (**Figure 9**). These results support the notion that membrane binding and polymerization are cooperative processes that are both required for efficient bactofilin assembly. Moreover, they suggest that membrane-bound client proteins can contribute to the recruitment of bactofilins to the cytoplasmic membrane, although the importance of this effect may vary between systems.

Discussion

Bactofilins are widespread among bacteria and mediate the spatial organization of diverse cellular processes. Although the polymers they form are typically associated with the inner face of the cytoplasmic membrane, the vast majority of bactofilin homologs lack transmembrane helices, suggesting the existence of an alternative membrane-targeting mechanism. Consistent with this notion, the membrane-binding activity of the bactofilin *Th*Bac from *T. thermophilus* has recently been localized to the unstructured N-terminal tail of the protein, and a sequence alignment based on several well-characterized bactofilin homologs suggested the existence of a conserved N-terminal motif in this protein region (Deng et al., 2019). Our work considerably extends these initial findings by determining the precise composition of the N-terminal MTS, unraveling its mode of action and clarifying its conservation among bacteria. Moreover, we reveal a mutual dependence of membrane-binding and bactofilin polymerization and provide first insights into mode of interaction between the bactofilin scaffold and membrane-associated client proteins.

Mutational analysis of *C. crescentus* BacA identified residues F2 and K4/K7 as key components of the BacA MTS (**Figure 1B**). This finding is explained by the results of our MD analysis, which show that the insertion of F2 into the hydrophobic core of the lipid bilayer (**Figure 5**) is critical to ensure the proper positioning of the MTS in the membrane, thereby promoting electrostatic interactions of the N-terminal NH_3^+ group with the negatively charged lipid headgroups of phosphatidylglycerol. The positively charged ε-amino groups of K4 and K7, by contrast, directly interact with these lipid headgroups, making the largest contribution to the overall interaction energy (**Figure 6**). Notably, the N-terminal methionine residue of proteins is usually removed after translation when followed by an amino acid with a short side chain (Hirel et al., 1989). In the case of BacA, however, the bulky phenylalanine residue at position 2 presumably inhibits this process, so that residue M1 may be a genuine, conserved part of the MTS. Although M1 interacts most extensively with the lipid bilayer (**Figure 6**), its absence has only a moderate effect on the membrane-binding activity of BacA *in vitro* (**Figure 3**). This observation supports the idea that most of its interaction energy is contributed by the N-terminal NH_3^+ group, whereas the insertion of the M1 side chain into the hydrophobic core of the membrane only serves to tune the positioning of the N-terminus at the lipid-water interface. Consistent with the results of the MD simulations, the loss of either F2 or K4/K7 drastically impairs the membrane-binding activity of BacA (**Figures 2C and 3**). Moreover, it prevents the assembly of BacA into distinct higher-order complexes (**Figure 1B**), suggesting a link between BacA membrane association and polymerization. Indeed, a soluble BacA variant lacking the native MTS (Δ2-8) regains the ability to form polymeric complexes when fused to a heterologous MTS from *E. coli* MreB (**Figure 4C**),

indicating that membrane binding is a prerequisite for efficient BacA polymerization. Conversely, polymerization appears to promote membrane binding, because the disruption of the BacA polymerization interface (F130R) strongly increases the fraction of soluble protein (**Figure 4**). Comparable results were obtained when a suitable membrane anchor was provided *in trans* (**Figure 9**). Together, these findings point to a cooperative binding mechanism, whereby (i) membrane association leads to an increase in the local concentration of BacA that facilitates its self-assembly into polymers, and (ii) polymerization closely juxtaposes multiple MTS-containing N-terminal tails, thereby increasing the avidity of BacA for the membrane and shifting the equilibrium to the membrane-bound state. This process may be particularly relevant at the low bactofilin levels (~200 BacA molecules per cell) found in *C. crescentus* cells (Kühn et al., 2010).

Interestingly, substitutions in the MTS that did not completely abolish BacA assembly often led to the formation of multiple and/or mislocalized complexes (**Figure 1–figure supplement 4**). The mechanism determining the polar localization of BacA is still unclear. However, it is conceivable that bactofilin polymers are intrinsically curved and thus preferentially associate with membrane regions of positive or negative Gaussian curvature (Kühn et al., 2010; Pöhl et al., 2024). Alternatively, the MTS may preferentially bind certain lipid species that are enriched in the polar regions of the cell, with its modification leading to a change in the lipid specificity that interferes with this recruitment pathway. Exchanges at less critical positions of the MTS may affect these recruitment mechanisms by reducing the membrane-binding affinity and thus, indirectly, also the dimensions of BacA polymers or by altering their lipid specificity.

To assess the conservation of mode of membrane association established for BacA, we conducted a comprehensive comparison of the N-terminal regions of all bactofilin homologs known to date. This analysis revealed that amino acid sequences similar to the MTS of BacA are highly prevalent in a large number of bactofilins from the phyla Pseudomonadota, Bacteroidota and Bacillota, strongly suggesting that MTS-mediated membrane binding is a common theme among this group of proteins (**Figure 7**). Notably, however, most prevalent N-terminal motifs identified for the bactofilin homologs of Spirochaetota and Thermodesulfobacteriota are fundamentally different from those of the other phyla investigated (**Figure 7 and Figure 7–figure supplement 2**), suggesting that they exhibit in a different mode of membrane binding or interact with factors other than the cytoplasmic membrane.

Notably, a small subset of bacterial bactofilin homologs contain an N-terminal transmembrane domain, which mediates their stable insertion into the cytoplasmic membrane. While found in a diversity of bacterial phyla, these proteins are particularly abundant in the Pseudomonadota, especially in their gamma-

proteobacterial and alphaproteobacterial lineages (**Figure 7–figure supplement 1**). One of them, the bactofilin CcmA of *P. mirabilis*, has been previously investigated (Hay et al., 1999). It was shown to undergo proteolytic processing and exist in two forms, a full-length form that is an integral membrane protein and a shorter form that lacks the N-terminal transmembrane segments. Intriguingly, the shorter form has an N-terminal sequence (MFSRKTE) that corresponds to the predicted consensus sequence of the MTS in Pseudomonadota and, indeed, behaves like a typical peripheral membrane protein. The specific functional properties conferred by these two distinct modes of membrane association are still unclear. However, it is tempting to speculate that the assembly of MTS-containing bactofilins may be dynamically regulated by cell cycle-dependent changes in membrane curvature or composition, whereas homologs with transmembrane domains may form more static polymeric assemblies. Consistent with this idea, *C. crescentus* BacA only assembles at the old cell pole once its cell envelope bulges outward to initiate stalk formation, thereby establishing a region of positive Gaussian curvature, although its cytoplasmic levels remain constant throughout the cell cycle (Kühn et al., 2010). Similarly, the BacA homolog of the stalked budding bacterium *H. neptunium* consistently assembles in regions of positive Gaussian curvature, first localizing to the stalked pole and then, once the terminal segment of the stalk starts to expand into a bud, to the bud neck (Pöhl et al., 2024).

Instead of using an MTS or a transmembrane domain, some bactofilins may also interact with the membrane indirectly by binding to other membrane-associated proteins, as recently suggested for the bactofilin homolog CcmA from *H. pylori* (Sichel et al., 2022). Our results suggest that the interaction with PbpC contributes, at least to some extent, to the membrane association of *C. crescentus* BacA. We did not observe any obvious localization defects in a Δ*pbpC* mutant (**Figure 8–figure supplement 1A**), indicating that PbpC binding is not critical for its proper assembly and positioning at native accumulation levels. However, when produced in excess, the PbpC membrane anchor was able to fully compensate for the absence of the N-terminal MTS, providing sufficient links with the cytoplasmic membrane to enable the assembly of polar BacA clusters. Thus, client protein binding is an important factor to consider when analyzing the assembly and localization dynamics of bactofilins *in vivo*.

The determinants mediating the interaction of membrane-associated bactofilin scaffolds with their client proteins are still poorly understood. For *M. xanthus* BacP, the binding site for its soluble interactor PadC was shown to be located in the exceptionally long unstructured C-terminal tail, which contains a conserved KKKVVVKK motif potentially involved in the interaction (Anand et al., 2020; Lin et al., 2017). However, most bactofilin homologs have much shorter C-terminal tails, which are typically poorly conserved in sequence and, at least in certain cases, dispensable for function *in vivo* (Sichel et al., 2022),

suggesting a direct interaction of client proteins with the bactofilin core domain. Our results indeed suggest that the cytoplasmic tail of PbpC associates with the C-terminal region of the bactofilin domain, close to the polymerization interface. Importantly, BacA assembly appears to be critical for efficient PbpC binding *in vitro* (**Figure 8C**), suggesting that inter-subunit contacts could potentially change the conformation of BacA such as to increase its affinity for its client protein. In addition, polymers may have a higher avidity for PbpC than BacA monomers. Polymerization thus acts as a trigger for both membrane association and the recruitment of client proteins, ensuring the tight regulation of bactofilin function.

Collectively, our findings provide important new insights into the function of bactofilins and the nucleotide-independent dynamics of their assembly. It will be interesting to analyze how cell cycle- or stress-induced changes in membrane composition affect the membrane-binding and polymerization behavior of MTS-containing bactofilin homologs. Moreover, it will be informative to shed light on the mode of membrane binding for bactofilins with conserved N-terminal sequences that are clearly distinct from the global consensus motif.

Material and methods

Media and growth conditions

C. crescentus CB15N and its derivates were grown aerobically at 28 °C in PYE rich medium (Poindexter, 1964), unless indicated otherwise. To induce stalk elongation, cells were cultivated for 24 h in M2G^{-P} medium (Kühn et al., 2010) prior to analysis. When required, media were supplemented with antibiotics at the following concentrations (mg ml^{-1} in liquid/solid media): kanamycin (5/25 µg/ml), streptomycin (5/5 µg/ml) or gentamicin (0.5/5 µg/ml). *E. coli* strains are grown aerobically at 37 °C in LB medium containing antibiotics at the following concentrations (mg ml^{-1} in liquid/solid media): ampicillin (200/200), chloramphenicol (20/30), gentamicin (0.5/5), kanamycin (30/50). To induce gene expression, media were supplemented with 0.005% or 0.03% D-xylose, 0.5 mM sodium vanillate or 1 mM IPTG, when appropriate.

Construction of plasmids and strains

The bacterial strains and plasmids used in this work are described in **Supplementary files 5** and **6**. The oligonucleotides used for their construction are listed in **Supplementary file 7**. All plasmids were verified by DNA sequencing. *C. crescentus* was transformed by electroporation (Ely, 1991). Non-replicating plasmids were integrated into the chromosome by single homologous recombination at the *xylX* locus (Thanbichler et al., 2007). Proper chromosomal integration was verified by colony PCR.

Live-cell imaging

To prepare samples for microscopy, overnight cultures were diluted to an OD_{600} of 0.1 and cultivated for 1 h prior to the addition of 0.005% D-xylose. After a further 1 h (BacA variants) or 2 h (PbpC variants) of incubation, the cultures were diluted tenfold and samples (1.5 µl) of the suspensions were spotted on 1% agarose pads prepared with double-deionized water. Images were taken with an Axio Observer.Z1 microscope (Zeiss, Germany) equipped with a Plan Apochromat 100x/1.45 Oil DIC, a Plan Apochromat 100x/1.4 Oil Ph3 M27 objective and a pco.edge 4.2 sCMOS camera (PCO, Germany). An X-Cite® 120PC metal halide light source (EXFO, Canada) and appropriate filter cubes (ET-CFP, ET-YFP or ET-TaxasRed; Chroma, USA) were used for fluorescence detection. Images were recorded with VisiView 3.3.0.6 (Visitron Systems, Germany) and processed with Fiji 2.14.0/1.54f (Schindelin et al., 2012) and Adobe Illustrator CS6 (Adobe Systems, USA). The subcellular distribution of fluorescence signals was analyzed with BacStalk (Hartmann et al., 2020).

Transmission electron microscopy

BacA or its mutant derivatives (2-3 mg/ml) were dialyzed overnight against TEM buffer (50 mM Tris-HCl (pH 8.0), 200 mM NaCl, 0.1 mM EDTA, 5% glycerol). Subsequently, 5 µl samples of the solutions were applied to glow-discharged carbon-coated grids (G2400C; Plano Wetzlar, Germany). After a brief incubition period, the grids were blotted with filter paper, washed with a droplet of double-distilled water and then treated for ~1 min with 2% (w/v) uranyl acetate before being blotted dry. Micrographs were taken with a JEM-2100 transmission electron microscope (JEOL, Japan) at an acceleration voltage of 120 kV. Images were captured with a 2k x 2k fast scan CCD camera F214 (TVIPS, Germany). Fiji 2.14.0/1.54f (Schindelin et al., 2012) was used for data analysis.

Single-particle tracking

For single-particle tracking, cells were cultivated in M2G minimal media at 28 °C. In the early exponential growth phase, the expression of genes placed under the control of the *xylX* (P_{xyl}) promoter was induced by the addition of 0.005% D-xylose. After another 3 h of incubation, cells were spotted on coverslips (25 mm diameter; Menzel Gläser, Germany) and covered with 1% agarose pads prepared with double-destilled water. All coverslips were cleaned before use by sonication in 2% (v/v) Hellmanex II solution (Hellma, Germany) for 30 min at 37 °C, followed by rinsing in distilled water and a second round of sonication in double-distilled water. Images were taken at 20-ms intervals by slimfield microscopy (Plank et al., 2009), using an Olympus IX-71 microscope equipped with a UAPON 100x/ NA 1.49 TIRF objective, a back-illuminated electron-multiplying charge-coupled device (EMCCD) iXon Ultra camera (Andor Solis, USA) in stream acquisition mode, and a LuxX 457-100 (457 nm, 100 mW) light-emitting diode laser (Omicron-Laserage Laserprodukte GmbH, Germany) as an excitation light source. The laser beam was focused onto the back focal plane and operated during image acquisition with up to 2 mW (60 W cm^{-2} at the image plane). Andor Solis 4.21 software was used for camera control and stream acquisition. Each single-particle tracking analysis was preceded by the acquisition of a phase contrast image. Subsequently, ~500 frames were acquired to bleach most fluorescent proteins in the cell and thus reach the single-molecule level. Subsequently, remaining and newly synthesized molecules were tracked over ~2,500 frames. Prior to analysis, the frames recorded before reaching the single-molecule level were removed from the streams using photobleaching curves as a reference, and the proper pixel size (100 nm) and time increment were adjusted in the imaging metadata using Fiji (Schindelin et al., 2012). Subsequently, cell meshes were determined using Oufti (Paintdakhi et al., 2016) and single particles were tracked with u-track 2.2.0 (Jaqaman et al., 2008). After the removal of all trajectories that were shorter than five steps, the diffusional behavior of the tracked particles was analyzed using SMTracker 2.0 (Oviedo-Bocanegra et al., 2021).

Cell fractionation analysis

Overnight cultures were diluted to an OD_{600} of 0.1 and grown for 2 h prior to the addition of D-xylose to a final concentration of 0.03%. The cells were further cultivated for 1 h (*bacA-mVenus* alleles) or 2 h (*creS-mNeonGreen*) to allow the expression of the genes of interest. Subsequently, cells from 5 ml culture were harvested by centrifugation, washed with 0.2 M Tris-HCl (pH 8.0) and stored at -80 °C. For further processing, the pelleted cells were resuspended in a buffer containing 60 mM Tris-HCl (pH 8.0), 0.2 M sucrose, 0.2 M EDTA, 100 µg ml^{-1} phenylmethylsulfonyl fluoride (PMSF) and 10 µg ml^{-1} DNase I and lysed by sonication at 30% amplitude for 7.5 min with alternating 10-s on and off phases (Model 120 Sonic Dismembrator; Fisher Scientific, USA). The lysates were centrifuged for 10 min at 4,000 ×g (4 °C) to remove incompletely lysed cells, followed by ultracentrifugation for 1 h at 133,000 ×g (4 °C) to separate the soluble and membrane-containing insoluble fractions. The supernatants were carefully removed, and the pellets were resuspended in an equal volume of 0.2 M Tris-HCl (pH 8.0). Both fractions were then subjected to immunoblot analysis with anti-FlgH, anti-MipZ and anti-GFP or anti-mNeonGreen antibodies.

Immunoblot analysis

Immunoblot analysis was performed as described previously (Thanbichler and Shapiro, 2006). Proteins were detected with a polyclonal anti-GFP antibody (Sigma, Germany; Cat. #: G1544; RRID: AB_439690), a monoclonal anti-mNeonGreen antibody (Chromotek, Germany; Cat. #: 32f6; RRID: AB_2827566), anti-MipZ antiserum (Thanbichler and Shapiro, 2006), anti-FlgH antiserum (Mohr et al., 1996) or a monoclonal anti-RFP antibody (MBL Life Science, Germany; Cat. #: M155-3) at dilutions of 1:10,000, 1:1,000, 1:10,000, 1:10,000 and 1:10,000, respectively. Goat anti-rabbit immunoglobulin G conjugated with horseradish peroxidase (Perkin Elmer, USA) or goat anti-mouse immunoglobulin G conjugated with horseradish peroxidase (Sigma, Germany) were used as secondary antibodies. Immunocomplexes were detected with the Western Lightning Plus-ECL chemiluminescence reagent (Perkin Elmer, USA). The signals were recorded with a ChemiDoc MP imaging system (BioRad, Germany) and analyzed using Image Lab software (BioRad, Germany).

Protein purification

To overproduce His_6-SUMO-BacA or mutant variants thereof, *E. coli* Rosetta(DE3)/pLysS cells transformed with the appropriate plasmids were grown overnight at 37 °C, diluted 100-fold into 3 l of LB medium containing antibiotics and cultivated to an OD_{600} of ~0.6. Subsequently, the media were supplemented with IPTG to a final concentration of 1 mM, and the cells were incubated for another 4 h before they were harvested by centrifugation and stored at -80 °C until further use. To purify the fusion proteins, the

pelleted cells were resuspended in buffer B (50 mM Tris/HCl pH 8.0, 300 mM NaCl, 0.1 mM EDTA, 5% glycerol and 20 mM imidazole) supplemented with 10 µg/ml DNase I and 100 µg/ml PMSF and lysed by three passages through a French press at 16,000 psi to break cells. The crude cell extract was cleared by centrifugation for 30 min at 16,000 ×rpm (4 °C) and loaded onto a 5 ml HisTrap™ HP affinity column (GE Healthcare, USA) equilibrated with buffer B with an ÄKTA Pure FPLC system (Cytiva). After washing of the column with 50 ml of buffer B, protein was eluted with a 50-ml linear gradient of imidazole (20-250 mM imidazole in buffer B). Fractions that were highly enriched in the protein of interest were supplemented with 200 µg Ulp1-His_6 protease (Marblestone et al., 2006) and dialyzed overnight at 4 °C against buffer C (50 mM Tris-HCl pH 8.0, 300 mM NaCl, 0.1 mM EDTA, 5% glycerol, 1 mM DTT) to cleave off the His_6-SUMO tag and remove the imidazole. Subsequently, the protein solution was again applied to a 5 ml HisTrap™ HP affinity column to separate the untagged BacA protein from His_6-SUMO and Ulp1-His_6. The flow-through fractions were collected and analyzed by SDS-PAGE. Fractions containing the desired protein in high amount and purity were dialyzed against buffer D (50 mM Tris-HCl pH 8.0, 200 mM NaCl, 0.1 mM EDTA, 5% glycerol) ($BacA_{\Delta 2\text{-}8}$) or buffer E (50 mM MOPS-NaOH pH 7.0, 200 mM NaCl, 0.1 mM EDTA, 5% glycerol) (all other BacA variants). The protein solutions were then concentrated using Amicon Ultra Centrifugal Filter (10 kDa MWCO) ultrafiltration devices (Millipore, Germany) and stored in small aliquots at -80 °C.

Size-exclusion chromatography

BacA or its F130R variant were diluted to a concentration of 1.5 mg/ml, applied to a Superdex 200 10/300 GL size-exclusion column (Cytiva, Germany) and eluted at a flow rate of 0.3 ml/min using an ÄKTA Pure FPLC system (Cytiva). Protein was detected by photometry at a wavelength of 280 nm.

Preparation of liposomes

Liposomes were generated from 1-palmitoyl-2-oleoyl-sn-glycero-3-phospho-(1'-rac-glycerol) (16:0-18:1 PG) (10 mg/mL in chloroform; Avanti Polar Lipids, USA). Chloroform was evaporated in a rotatory evaporator, resulting in a lipid film that was left to dry overnight. Subsequently, the lipids were resuspended in liposome buffer (50 mM MOPS-NaOH pH 7.0, 200 mM NaCl), and the mixture was incubated at room temperature for 1 h with periodic vigorous agitation. To prepare small unilamellar vesicles (SUVs) with an average diameter of 100 nm, the final lipid solution (20 mg ml^{-1}) was extruded at least ten times through a Mini Extruder (Avanti Polar Lipids, USA) equipped with polycarbonate membranes of 0.1 µm pore size, until the solution was clear.

Co-sedimentation assay

Protein (20 µM) was incubated for 20 min at room temperature with or without liposomes (0.4 mg ml^{-1}) in binding buffer (50 mM MOPS-NaOH pH 7.0, 300 mM NaCl) in a total reaction volume of 100 µl. The mixtures were then centrifuged for 20 min at 100,000 ×g (20 °C) in a TLA-55 rotor (Beckman Coulter, Germany). After transfer of the supernatant to a reaction tube and resuspension of the pellet in 100 µl of liposome buffer (50 mM MOPS-NaOH pH 7.0, 200 mM NaCl), samples of the two fractions were mixed with SDS-PAGE sample buffer, heated at 95 °C for 10 min and loaded onto a 15% SDS-polyacrylamide gel. After electrophoresis, protein was stained with Coomassie Brilliant Blue R-250. The gels were imaged in a ChemiDoc MP imaging system (BioRad, Germany) using Image Lab software (BioRad, Germany), and the intensity of protein bands was quantified using Fiji 2.14.0/1.54f (Schindelin et al., 2012).

Bio-layer interferometry

Bio-layer interferometry experiments were conducted using a BLItz system equipped with Octet® High Precision Streptavidin 2.0 (SAX2) Biosensors (Satorius, Germany). In the initial step, an N-terminally biotinylated $PbpC_{1\text{-}13}$ peptide (Biotin-Ahx-MNDWTLPPYKFDD; GenScript, USA) was immobilized on the sensor. After the establishment of a stable baseline, association reactions were monitored with BacA at various concentrations or with different BacA variants of the same concentration. At the end of each binding step, the sensor was transferred into an analyte-free buffer to measure the dissociation kinetics. The extent of non-specific binding was assessed by monitoring the interaction of the analyte with unmodified sensors. All analyses were performed in BLItz binding buffer (50 mM MOPS/NaOH pH 7.0, 100 mM NaCl, 1 mM EDTA, 5% glycerol, 10 µM BSA, 0.01 % Tween)

Hydrogen-deuterium exchange mass spectrometry

Samples were prepared using a two-arm robotic autosampler (LEAP technologies, Denmark). 7.5 µl of BacA (25 µM) or a mixture of BacA (25 µM) and $PbpC_{aa1\text{-}13}$ (100 µM) were mixed with 67.5 µl of D_2O-containing buffer (20 mM HEPES-NaOH pH 8.0, 300 mM NaCl) to start the exchange reaction. After 10, 100, 1,000 and 10,000 sec of incubation at 25 °C, 55 µl samples were taken from the reaction and mixed with an equal volume of quench buffer (400 mM KH_2PO_4/H_3PO_4, 2 M guanidine-HCl, pH 2.2) kept at 1 °C. 95 µl of the resulting mixture were immediately injected into an ACQUITY UPLC M-class system with HDX technology (Waters™, USA) (Wales et al., 2008). Undeuterated samples of BacA and a mixture of BacA and $PbpC_{1\text{-}13}$ were prepared similarly by 10-fold dilution into H_2O-containing buffer. Proteins were digested online on an Enzymate BEH Pepsin column (300 Å, 5 µm, 2.1 mm × 30 mm; Waters™, USA) at 12 °C with a constant flow (100 µl min^{-1}) of 0.1 % (v/v) formic acid in water, and the resulting peptic peptides

were collected on a trap column (2 mm × 2 cm) that was filled with POROS 20 R2 material (Thermo Fisher Scientific, USA) and kept at 0.5 °C. After 3 min, the trap column was placed in line with an ACQUITY UPLC BEH C18 1.7 µm 1.0 × 100 mm column (Waters™, USA), and the peptides were eluted at 0.5 °C using a gradient of 0.1 % (v/v) formic acid in water (A) and 0.1 % (v/v) formic acid in acetonitrile (B) at a flow rate of 30 µl/min generated as follows: 0-7 min/95-65 % A, 7-8 min/65-15 % A, 8-10 min/15 % A, 10-11 min/5 % A, 11-16 min/95 % A. Peptides were ionized with an electrospray ionization source operated at 250 °C capillary temperature and a spray voltage of 3.0 kV. Mass spectra were acquired over a range of 50 to 2,000 m/z on a G2-Si HDMS mass spectrometer with ion mobility separation (Waters™, USA) in Enhanced High Definition MS ($HDMS^E$) or High Definition MS (HDMS) mode for undeuterated and deuterated samples, respectively. A [Glu1]-Fibrinopeptide B standard (Waters™, USA) was employed for lock mass correction. After each run, the pepsin column was washed three times with 80 µl of 4 % (v/v) acetonitrile and 0.5 M guanidine hydrochloride, and blanks were performed between each sample. All measurements were carried out in triplicate.

Peptides from the non-deuterated samples (acquired with $HDMS^E$) were identified with the ProteinLynx Global SERVER (PLGS, Waters™, USA), employing low energy, elevated energy and intensity thresholds of 300, 100 and 1000 counts, respectively. Peptides were matched using a database containing the amino acid sequences of the proteins of interest, pepsin and their reversed sequences. The search parameters were as follows: peptide tolerance = automatic; fragment tolerance = automatic; min fragment ion matches per peptide = 1; min fragment ion matches per protein = 7; min peptide matches per protein = 3; maximum hits to return = 20; maximum protein mass = 250,000; primary digest reagent = non-specific; missed cleavages = 0; false discovery rate = 100. Deuterium incorporation was quantified with DynamX 3.0 (Waters™, USA), using peptides that fulfilled the following criteria: minimum intensity = 5,000 counts; maximum length = 40 amino acids; minimum number of products = 2; maximum mass error = 25 ppm; retention time tolerance = 0.5 min. After automated data processing with DynamX, all spectra were manually inspected and, if necessary, peptides were omitted (e.g. in case of a low signal-to-noise ratio or the presence of overlapping peptides).

Bioinformatic analysis

Nucleotide and protein sequences were obtained from the National Center for Biotechnology Information (NCBI) or UniProt (UniProt Consortium, 2023) databases, respectively. Sequences were compared and analyzed using the blastn, blastp or PSI-blast algorithm as implemented on the NCBI website. The presence of putative amphipathic helices was assessed using AMPHIPASEEK (Sapay et al., 2006). Multiple sequence

alignments were generated with MUSCLE v3.8.31 (Edgar, 2004) and viewed and edited with Jalview v2 (Waterhouse et al., 2009).

To identify conserved motifs in the N-terminal regions of bactofilins, all known bactofilin homologs were retrieved from the UniProt database (UniProt Consortium, 2023). Subsequently, a Python-based pre-processing procedure was used to exclude non-bacterial entries, remove sequences with predicted trans-membrane helices and eliminate sequences from species with unclear phylogeny. In addition, highly similar sequences (with over 90% similarity) from the same species were filtered out to correct biases due to over-sequencing. The N-terminal region of each protein was determined using hmmscan (HMMER 3.3.2) (Eddy, 2011) with the hidden Markov profile constructed from the seed alignment of the bactofilin domain downloaded from the Pfam database (Paysan-Lafosse et al., 2022). Subsequently, sequences with N-terminal regions shorter than 8 amino acids were eliminated. The resulting set of sequences was categor-ized by phylum, and MEME (Bailey and Elkan, 1994) was used to detect the 10 most probable motifs. The analysis employed the following settings: classical objective function, with zero or one occurrence per sequence, motif width ranging from 5 to 50 amino acids, and a 0^{th}-order background Markov model.

Molecular dynamics simulations

All molecular dynamics (MD) simulations were carried out with Gromacs (version 2021.1) (Abraham et al., 2015). The simulation systems were set up and prepared for MD simulation with the Charmm-GUI (Jo et al., 2008; Jo et al., 2009; Lee et al., 2016; Wu et al., 2014),using the Charmm36m force field (Huang et al., 2017) for the peptide and lipids together with the Charmm-specific TIP3P water model. The lipid composi-tion of the simulated bilayer (**Supplementary file 2**) was chosen such that it mimics as closely as possible the *C. crescentus* membrane (Chow and Schmidt, 1974; De Siervo and Homola, 1980). Symmetric bilayers with 128 lipids in each monolayer were constructed, that is, the same number and type of lipids was present in the two leaflets. At the beginning of the simulations, a single bactofilin 10-mer peptide (either the wild-type sequence MFSKQAKSNN, or the K4SK7S or F2Y mutants) were modeled as extended con-formations and placed in the bulk water phase, located at least 3 nm away from the lipid headgroups. The net charge of the simulation box was neutralized with 150 mM KCl. After energy minimization (with steepest descent), MD simulations were carried out with periodic boundary conditions in the NpT ensemble at a constant temperature of 310 K, maintained via the Bussi velocity-rescaling thermostat (Bussi et al., 2007), and constant 1 bar pressure, maintained by semi-isotropic pressure coupling of the lateral (x,y) and normal (z) dimensions of the simulation box to a weak coupling barostat (Berendsen et al., 1984). Short-range Coulomb and Lennard-Jones 6,12 interactions were described with a buffered pair

list (Páll and Hess, 2013) with potentials smoothly shifted to zero at a 1.2 nm distance, with forces switched to zero between 1.0 and 1.2 nm. The long-range electrostatic interactions were described with the particle mesh Ewald (PME) method with 0.12 nm grid spacing (Darden et al., 1993). The LINCS and SETTLE algorithms were used to constrain all protein bonds involving H-atoms and to keep the water molecules rigid, respectively, allowing to integrate the equations of motion with 2 fs time steps using the leap-frog integrator. The final production MD simulations were 500 ns long.

Data analysis

Data were analyzed in Excel 2019 (Microsoft) or Python 3.10.12 and mainly visualized using the Python Matplotlib v3.6.2 (Hunter, 2007) and Seaborn v0.12.2 (Waskom, 2021) libraries. The plots obtained were edited with Adobe Illustrator CS6 (Adobe Systems) to generate the final figures.

Statistics and reproducibility

All experiments were performed at least twice independently with similar results. No data were excluded from the analyses. To quantify imaging data, multiple images were analyzed per condition. The analyses included all cells in the images or, in the case of high cell densities, all cells in a square portion of the images. The selection of the images and fields of cells analyzed was performed randomly.

Availability of biological material

The plasmids and strains used in this study are available from the corresponding author upon request.

Data availability

All data generated in this study are included in the manuscript and the supplementary material.

Acknowledgements

We thank Julia Rausch for excellent technical assistance.

Additional information

Funding

Funder	Grant reference number	Author
University of Marburg	Core funding	Martin Thanbichler Gert Bange
Max Planck Society	Max Planck Fellowship	Martin Thanbichler
Max Planck Society	Max Planck Fellowship	Gert Bange
German Research Foundation (DFG)	450420164 – TH 885/3-1	Martin Thanbichler
German Research Foundation (DFG)	EXC 2033 – 390677874 – RESOLV	Lars V. Schäfer
German Research Foundation (DFG)	324652314	Gert Bange
German Research Foundation (DFG)	260989694	Gert Bange
European Union's Horizon 2020 research and innovation program	Marie Skłodowska-Curie grant agreement No 801459 – FP-RESOMUS	Saumyak Mukherjee
Max Planck Society	Postdoctoral research grant from the Microcosm Earth Center	Rogelio Hernández-Tamayo

The funders had no role in the design of the study, the collection and interpretation of the data, or the decision to submit the work for publication.

Data availability

All relevant data generated in this study are included in the manuscript, the supplemental information, and the Source Data file.

Competing interests

The authors declare no competing interests.

Author contributions

Ying Liu: Conceptualization, methodology, validation, investigation, formal analysis, visualization, writing–original draft, writing–review and editing; constructed strains, performed cell biological and biochemical studies and conducted the bioinformatic analyses. **Rajani Karmakar**: investigation, formal analysis, visualization, writing–review and editing; conducted the MD simulations. **Maria Billini**: investigation, formal analysis, visualization, writing–review and editing; constructed strains and performed cell biological and biochemical studies. **Wieland Steinchen**: investigation, formal analysis, visualization, writing–review and editing; performed the HDX mass spectrometry analysis. **Saumyak Mukherjee**: supervision, formal analysis, writing–review and editing; contributed to the analysis of the MD simulations. **Rogelio Hernández-**

Tamayo: investigation, formal analysis, visualization, writing–review and editing; performed the single-particle tracking analysis. **Thomas Heimerl**: investigation, formal analysis, visualization, writing–review and editing; conducted the transmission electron microscopy analysis. **Gert Bange**: supervision, funding acquisition, writing–review and editing. **Lars V. Schäfer**: supervision, formal analysis, funding acquisition, writing–original draft, writing–review and editing; supervised the MD simulations and contributed to the analysis of the data obtained. **Martin Thanbichler**: conceptualization, supervision, formal analysis, visualization, funding acquisition, writing–original draft, writing–review and editing.

Figure legends

Figure 1. Identification of residues critical for the membrane-binding activity of BacA *in vivo*. (A) Schematic representation of the BacA-mVenus fusion protein used in this study. The proposed membrane-targeting sequence is highlighted in red. The sequence at the bottom shows that result of an amphipathic helix prediction for BacA using the AMPHIPASEEK software (Sapay et al., 2006). Residues predicted to be located in an unstructured, randomly coiled region are labeled with "c". **(B)** Localization patterns of mutant BacA-mVenus variants. Δ*bacAB* cells producing BacA-mVenus or mutant variants thereof (strains LY84, LY89, LY90, LY97, LY111, LY112, LY113, LY119) were analyzed by phase contrast and fluorescence microscopy. The outlines of the cells are shown in the fluorescence images. Demographs summarizing the single-cell fluorescence profiles obtained from random subpopulations of cells are given next to the respective fluorescence images. The numbers of cells analyzed are: WT (130), Δ2-8 (292), F130R (156), F2Y (138), F2E (194), K4S-K7S (151), K4E-K7E (382), F2E-K4E-K7E (130). The vertical red line indicates the junction between cell body and the stalk. Scale bar: 2 µm. **(C)** Helical wheel diagram of the first eight amino acids of BacA. Residues are colored by properties: hydrophobic (gray), basic (blue), uncharged (yellow).

Figure 1–figure supplement 1. Ultrastructure of different BacA variants. Wild-type BacA, its MTS-free Δ2-8 variant and its polymerization-deficient F130R variant (xx mg/ml) were stained with uranyl acetate and visualized by transmission electron microscopy. Bar: 100 nm.

Figure 1–figure supplement 2. Size-exclusion chromatography analysis of wild-type BacA and its F130R variant. The indicated proteins were applied to a Superdex 200 size-exclusion column and detected photometrically at a wavelength of 280 nm. The following standard proteins were analyzed as a reference to calibrate the column: Thyroglobulin (669 kDa), Ferritin (440 kDa), Aldolase (158 kDa), Conalbumin (75 kDa), Ovalbumin (44 kDa), Ribonuclease A (14 kDa).

Figure 1–figure supplement 3. Stability of different BacA-mVenus variants. Derivates of strain JK5 (Δ*bacAB*) carrying the indicated alleles of *bacA-mVenus* under the control of the xylose-inducible P_{xyl} promoter were grown overnight, diluted to an OD_{600} of ~ 0.1 and incubated for another hour. The strains were then induced with 0.03% xylose for 1 h and subjected to immunoblot analysis with an anti-GFP antibody. Strain JK5 was analyzed as a negative control (NC). The positions of standard proteins (in kDa) are indicated on the left side of the images.

Figure 1–figure supplement 4. Localization patterns of different BacA-mVenus variants. Δ*bacAB* cells producing the indicated BacA-mVenus variants (strains LY95, LY88, LY96, LY91, LY92) were analyzed by phase contrast and fluorescence microscopy. The outlines of the cells are shown in the fluorescence images. Demographs summarizing the single-cell fluorescence profiles obtained from random subpopulations of cells are given next to the respective fluorescence images. The numbers of cells analyzed are: S3A (109), K4S (150), Q5A (121), A6S (184), K7S (128). The vertical red line indicates the junction between cell body and the stalk. Scale bar: 2 µm.

Figure 2. Verification of residues M1, F2 and K4/K7 as critical components of the BacA MTS. (A) Mobility of the indicated BacA-mVenus fusion proteins. Shown is the average mean-squared displacement (MSD) (± SD) as a function of time, based on single-particle tracking analysis. The fitted lines were obtained by linear regression analysis. **(B)** Cell fractionation experiment investigating the membrane-binding activity of BacA-mVenus (WT) or a mutant variant lacking the predicted MTS (Δ2-8). Whole-cell lysates (W) as well as the soluble (S) and pellet (P) fractions of cells producing the indicated proteins were subjected to immunoblot analysis with an anti-GFP antibody, detecting the BacA-mVenus fusion protein. As controls, the same samples were probed with antibodies raised against the soluble cell division regulator MipZ (Thanbichler and Shapiro, 2006) or the membrane-bound flagellar L-ring subunit FlgH (Mohr et al., 1996) from *C. crescentus*. **(C)** As in panel B, but for cells producing mutant BacA-mVenus variants with single or multiple amino-acid exchanges in the predicted MTS. Shown are representative images (n=3 independent replicates). The strains used are given in the legend to Figure 1B.

Figure 2–figure supplement 1. Subcellular localization of the single-molecule tracks obtained for different BacA-mVenus variants. The single-particle tracks determined for wild-type BacA-mVenus, free mVenus and the indicated BacA-mVenus variants were mapped onto phase contrast images of the cells in which they were recorded. The images show the results obtained from representative cells. Red lines indicate slow-moving particles, green lines indicate fast-moving particles (as defined in **Supplementary file 1**). Bar: 1 µm.

Figure 2–video 1. Single-particle dynamics of different BacA-mVenus variants. The movies show the single-particle dynamics of wild-type BacA-mVenus, free mVenus and the indicated BacA-mVenus variants in representative cells. The outlines of the cells are indicated in white. Red lines show the tracks of individual particles. Images were acquired at 20-ms intervals. Bar: 1 µm.

Figure 3. Co-sedimentation analysis of the association of various BacA variants with liposomes. The indicated proteins (20 µM) were incubated without (-) or with (+) liposomes (0.4 mg/mL) prior to ultra-centrifugation. The supernatant and pellet fractions of each mixture were analyzed by SDS gel electro-phoresis. Shown are scans of representative gels and a quantification of the average relative signal intensities (± SD) obtained for the different fractions (n=3 independent replicates).

Figure 4. Interplay between BacA assembly and membrane binding. (A) Cell fractionation experiment investigating the membrane-binding activity of the polymerization-deficient F130R variant of BacA-mVenus *in vivo* (LY119). The analysis was performed as described for **Figure 2B**. **(B)** Co-sedimentation analysis of the association of BacA-F130R with liposomes *in vitro*, performed as described for **Figure 3**. **(C)** Role of polymerization in the membrane association of a BacA-mVenus variant carrying the membrane-targeting sequence of *E. coli* MreB. Shown are phase contrast and fluorescence images of Δ*bacAB* mutants (LY103, LY123) producing either a BacA-mVenus variant in which the MTS is replaced by two tandem copies of the N-terminal amphiphilic helix of *E. coli* MreB (^{MreB}WT) or a polymerization-deficient variant thereof (^{MreB}F130R). Demographs summarizing the single-cell fluorescence profiles obtained from random subpopulations of cells are given next to the respective fluorescence images. The numbers of cells analyzed are: ^{MreB}WT (126), ^{MreB}F130R (169). The vertical red line indicates the junction between cell body and the stalk. Scale bar: 2 µm. **(D)** Mobility of the indicated BacA-mVenus fusion proteins. Shown is the average mean-squared displacement (MSD) (± SD) as a function of time, based on single-particle tracking analysis. The mVenus, Δ2-8 and WT data are taken from **Figure 2A** and shown for comparison. **(E)** Cell fractionation experiment investigating the membrane-binding activity of ^{MreB}BacA-mVenus (^{MreB}WT) and its polymerization-deficient F130R variant (^{MreB}F130R) *in vivo* (LY103, LY123). The analysis was performed as described for **Figure 2B.**

Figure 4–figure supplement 1. Solubility of different CreS-mNeonGreen variants. (A) Schematics showing the CreS-mNeonGreen variants analyzed in this study. The membrane-targeting regions of CreS and BacA are shown in blue and red, respectively. **(B)** Cell fractionation experiment investigating the membrane-binding activity of CreS-mNeonGreen (WT) or mutant variants lacking the predicted membrane-targeting region (Δ27) or containing the BacA MTS instead of the native membrane-targeting region (^{BacA}CreS). Whole-cell lysates (W) as well as the soluble (S) and pellet (P) fractions of cells producing the indicated proteins were subjected to immunoblot analysis with an anti-mNeonGreen antibody. As controls, the same samples were probed with antibodies raised against the soluble cell division regulator MipZ (Thanbichler and Shapiro, 2006) or the membrane-bound flagellar L-ring subunit FlgH (Mohr et al.,

1996) from *C. crescentus*. Shown are representative images (n=3 independent replicates). **(C)** Quantification of the relative amounts of CreS-mNeonGreen or its mutant variants in the soluble and pellet fractions. The intensities of the signals obtained for the soluble and pellet fractions in the analysis described in panel B were quantified and normalized to the total intensity in these two fractions. Data represent the average (± SD) of three independent replicates.

Figure 5. Molecular dynamics simulation of the interaction between the BacA MTS and a model membrane. (A) Snapshot of the molecular dynamics (MD) simulation system showing the 10-mer peptide MFSKQAKSNN ($BacA_{1-10}$; red) after binding to the lipid bilayer. The water is shown in surface representation. K^+ and Cl^- counterions are not shown. **(B)** Close-up view of a representative snapshot from the MD simulation visualizing the binding mode of the peptide on the membrane surface. **(C)** Structural overlay of 40 snapshots from the MD simulation, taken after constant time intervals from the trajectory. **(D)** Density profiles of individual residues in the wild-type peptide along the membrane normal, i.e. the z-component of the distance vector from the center-of-mass (COM) of the bilayer, with the membrane midplane located at zero. The vertical dashed black line indicates the maximum of the density distribution of the lipid headgroup phosphates.

Figure 5–figure supplement 1. Density profiles for different MTS variants determined by molecular dynamics simulation. Density profiles of individual residues in the **(A)** wild-type, **(B)** F2Y and **(C)** K4S-K7S peptides along the membrane normal. The vertical dashed black line indicates the maximum of the density distribution of the lipid headgroup phosphates. The data shown in panel A are reproduced from **Figure 5D** for comparison.

Figure 6. Contact numbers and interaction energies for different peptide-lipid bilayer interactions. (A) The graph shows the total number of contacts between individual residues in the wild-type, K4S-K7S and F2Y peptides and the lipid bilayer as well as the number of contacts with PG lipids and GLY lipids. A contact between a peptide residue and a lipid was defined to exist if any two non-hydrogen atoms of the residue and a lipid molecule were within a distance of 0.5 nm to each other. Contacts were counted for each frame of the MD trajectories and averaged. Multiple contacts between a peptide and a lipid molecule were treated as a single contact, so that the number of contacts counted was either 1 or 0. The statistical errors plotted were obtained from the difference between the two different sets of 500-ns simulations, starting with peptides in an unfolded or α-helical conformation, respectively. **(B)** Energies of the interactions between individual residues in the wild-type, K4S-K7S and F2Y peptides and the lipid bilayer. The

interaction energies plotted are the combined interaction energies of all Coulomb and van-der-Waals interactions in the force field averaged over the simulation trajectories.

Figure 7. Conservation of the N-terminal regions of bactofilin homologs in different bacterial phyla. The pie chart in the middle shows the relative distribution of the 14337 unique bactofilin homologs analyzed among the indicated bacterial phyla. The sequence logos give the most widespread N-terminal motifs obtained either by a global analysis of all 14337 bactofilin sequences (global consensus) or by an analysis of subsets of these sequences from specific phyla.

Figure 7–figure supplement 1. Assessment of the conservation of the bactofilin membrane-targeting sequence. (A) Analysis pipeline used to analyze the conservation of the N-terminal regions among bacterial bactofilin homologs. **(B)** Relative abundance of annotated bactofilin homologs in the different domains of life. **(C)** Abundance of bactofilins with predicted transmembrane helices in different bacterial lineages. **(D)** Distribution of bactofilin homologs without predicted transmembrane helices among different bacterial phyla. Small phyla contributing less than three percent of the total number of sequences have been aggregated in the category 'Others'.

Figure 7–figure supplement 2. Conserved N-terminal motifs in bactofilin homologs from different phyla. The sequence logos give the most frequent N-terminal motifs obtained either by a global analysis of all 14,337 bactofilin sequences (global consensus) or by an analysis of subsets of these sequences from specific phyla. The number of bactofilin homologs that show N-terminal sequences corresponding to a specific motif and the likelihood for the existence of this motif are indicated on the left side of each sequence logo.

Figure 8. Interaction of BacA with its client protein PbpC. (A) Localization patterns of different PbpC variants. Δ*bacB* Δ*pbpC* cells producing mVenus-PbpC (LY75) or mutant variants thereof lacking region C1 (LY76) or carrying an unstructured region from *C. crescentus* DipM in place of the unstructured region connecting region C1 and the transmembrane helix (LY77) were analyzed by phase contrast and fluorescence microscopy. The outlines of the cells are shown in the fluorescence images. Demographs summarizing the single-cell fluorescence profiles obtained from random subpopulations of cells are given next to the respective fluorescence images. The numbers of cells analyzed are: LY75 (158), LY76 (253), LY77 (119). Scale bar: 2 µm. **(B)** Biolayer interferometric analysis of the interaction between $PbpC_{1\text{-}13aa}$ and BacA. A synthetic peptide comprising the first 13 amino acids of PbpC ($PbpC_{1\text{-}13}$) was immobilized on a biosensor and probed with increasing concentrations of BacA. After the association step, the sensor was transferred

to a protein-free buffer to monitor the dissociation reaction. The graph shows a representative titration series (n=3 independent replicates). **(C)** Comparison of the interaction of $PbpC_{aa1-13}$ with BacA and its polymerization deficient F130R variant, performed as described in panel B. **(D)** Mapping of the PbpC binding site on BacA by hydrogen-deuterium exchange (HDX) mass spectrometry. The plots show the extent of deuterium uptake by three representative peptides obtained after peptic digestion of BacA protein (2.5 µM) that had been incubated in the absence or presence of the $PbpC_{1-13}$ peptide (10 µM) for the indicated time periods (see **Supplementary file 4** for the full set of peptides). **(E)** Mapping of the differences in deuterium uptake observed at t=1000 s onto the solid-state NMR structure of BacA (Shi et al., 2015).

Figure 8–figure supplement 1. Localization patterns of mVenus-PbpC and BacA-Venus in different strain backgrounds. (A) Localization of mVenus-PbpC in the Δ*bacB* Δ*pbpC* (LY75) and the Δ*bacA* Δ*pbpC* (LY72) backgrounds. **(B)** Localization of BacA-Venus in the wild-type (MT256) and Δ*pbpC* (JK136) backgrounds. Cells were analyzed by phase contrast and fluorescence microscopy. The outlines of the cells are shown in the fluorescence images. Demographs summarizing the single-cell fluorescence profiles obtained from random subpopulations of cells are given next to the respective fluorescence images. The numbers of cells analyzed are: LY75 (158), LY72 (697), MT256 (264), JK136 (222). Scale bar: 1 µm.

Figure 8–figure supplement 2. Sequence alignment of the cytoplasmic tail of PbpC homologs. The schematic at the top shows the structure of PbpC. Conserved domains are shown in different colors. The cytoplasmic tail of PbpC comprises conserved Region C1 (aa 1-13), a proline-rich region (aa 14-62), conserved Region C2 (aa 63-70), and a region rich in positively charged amino acids (aa 71-83), located adjacent to the transmembrane helix. Abbreviations: TG: transglycosylase domain, TP: transpeptidase domain. The NCBI identifiers of the proteins analyzed are given on the left.

Figure 8–figure supplement 3. Stability of the mVenus-PbpC fusion proteins used in this study. Δ*bacB* Δ*pbpC* cells producing wild-type mVenus-PbpC (WT; LY75), an mVenus-PbpC variant lacking the conserved region C1 (Δ2-13; LY76) or an mVenus-PbpC variant containing an unstructured region from *C. crescentus* DipM in place of the unstructured region in between regions C1 and C2 (chimera; LY77) were grown overnight, diluted to an OD_{600} of ~0.1 and incubated for another hour. Subsequently, the cells were induced for 1.5 h with 0.3 % xylose and subjected to immunoblot analysis with an anti-GFP antibody. A Δ*bacAB* mutant producing BacA-mVenus and the wild-type strain CB15N (NC) were analyzed as positive and negative controls, respectively. The positions of standard proteins (in kDa) are indicated on the left of image.

Figure 8–figure supplement 4. Relevance of BacA binding for the localization and functionality of PbpC under phosphate-limiting conditions. (A) Phase contrast and fluorescence images of the *C. crescentus* wild-type (WT), a Δ*bacB* Δ*pbpC* mutant (LY71) and a Δ*bacB* Δ*pbpC* mutant producing either mVenus-PbpC (LY75) or an N-terminally truncated variant thereof lacking region C1 (Δ2-13; LY76) under the control of a xylose-inducible promoter after 24 h of cultivation in phosphate-limited ($M2G^{-P}$) medium containing 0.3% xylose. The demographs at the bottom show the fluorescence profiles of a representative subpopulation of cells stacked on top of each other and sorted according to cell length. The numbers of cells analyzed are: 428 (WT), 415 (LY71), 659 (LY75), 753 (LY76). Bar: 3 µm. **(B)** Quantification of stalk lengths in the cultures described in panel A. Shown are bee swarm plots of the data. The red dot indicates the median, the lines indicate the standard deviation. **(C)** Stability of the indicated mVenus-PbpC variants under phosphate starvation. The indicated strains were cultivated for 24 h in phosphate-limited medium in the absence (uninduced) or presence (induced) of 0.3% xylose and subjected to immunoblot analysis with an anti-GFP antibody. The positions of mVenus-PbpC and free mVenus are indicated on the right.

Figure 8–figure supplement 5. Biolayer interferometry analysis of the interaction between $PbpC_{aa1-13}$ and BacA. (A) Control showing the interaction of wild-type BacA (50 µM) with an unmodified biosensor. **(B)** Affinity of BacA for the immobilized $PbpC_{1-13}$ peptide. The final wavelength shifts measured for the different association curves in **Figure 8B** were plotted against the corresponding BacA concentrations. Data represent the average (± SD) of three independent replicates.

Figure 8–figure supplement 6. Mapping of the PbpC-binding site of BacA by hydrogen-deuterium-exchange (HDX) analysis. (A) Schematic showing the domain structure of BacA. **(B)** HDX analysis of BacA. Purified BacA (2.5 µM) was incubated in deuterated buffer for the indicated time intervals either alone (Apo) or in the presence of $PbpC_{1-13}$ peptide (10 µM). Shown is the degree of HDX along the primary sequence of BacA in the indicated conditions. The color scale is given on the right. The schematic at the top displays the predicted secondary structure of BacA. The black bars represent peptides of BacA that were analyzed for HDX. Residue-specific HDX information was obtained from these overlapping peptides by using the shortest peptide covering a given residue. Gaps indicate amino acid sequences not covered by any peptide. **(C)** HDX difference map. Shown are the residue-specific differences in HDX between BacA in the presence of $PbpC_{1-13}$ peptide and BacA alone that were obtained after the indicated incubation times. The data are projected onto the primary sequence of BacA. The color code is given on the right. Blue color denotes regions showing reduced HDX in the presence of $PbpC_{1-13}$.

Figure 9. Contribution of PbpC to BacA membrane association. *C. crescentus* Δ*bacAB* Δ*pbpC* cells producing the indicated BacA-mVenus variants (WT, Δ2-8, F130R) under the control of a xylose-inducible promoter and $PbpC_{1-132}$-mCherry under the control of a vanillate-inducible promoter (strains MAB575, MAB576 and MAB577) were grown in the presence of xylose (left) or both xylose and vanillate (right) prior to microscopic analysis. The images show representative fluorescence micrographs, with the cell outlines indicated in white. Arrowheads indicate polar $PbpC_{1-132}$-mCherry foci. Demographs summarizing the single-cell BacA-mVenus fluorescence profiles obtained from random subpopulations of cells are provided next to the respective fluorescence images. The number of cells analyzed is shown in the top left-hand corner of each graph. The schematics on top illustrate the protein constructs used for the analysis (not to scale). Bar: 3 µm.

Figure 9–figure supplement 1. Levels and stability the fluorescent fusion proteins used in colocalization studies. *C. crescentus* Δ*bacAB* Δ*pbpC* cells producing the indicated BacA-mVenus variants under the control of a xylose-inducible promoter and $PbpC_{1-132}$-mCherry under the control of a vanillate-inducible promoter (strains MAB575, MAB576 and MAB577) were grown in the presence of xylose (xyl) and/or vanillate (van) and subjected to immunoblot analysis with anti-GFP and anti-mCherry antibodies. The cells analyzed were from the same cultures as those in **Figure 9**. The positions of the fusion proteins and of the corresponding free fluorescent proteins are shown on the right.

Supplementary file legends

Supplementary file 1. Diffusion constants of different BacA-mVenus variants. The table shows the number of cells and tracks analyzed in the single-particle tracking studies as well as the diffusion coefficients obtained for each of the proteins investigated (Microsoft Word, DOCX file).

Supplementary file 2. Composition of the lipid bilayer in the MD simulations. The table shows the type, charge, fatty acid composition, percentage share and number count of the lipids in each of the two leaflets that constitute the lipid bilayer in the molecular dynamics (MD) simulations (Microsoft Word, DOCX file).

Supplementary file 3. Representative snapshot from an MD simulation visualizing the interaction of the wild-type $BacA_{1-10}$ peptide with a model lipid bilayer. The file gives the structural coordinates of the snapshot shown in **Figure 5B** (PDB file).

Supplementary file 4. Detailed description of the HDX data. The spreadsheets give a summary of the conditions used for the HDX analysis and a full list of the peptides obtained in the different experiments (Microsoft Excel, XLSX file).

Supplementary file 5. Strains used in this study. The table gives the genotypes, mode of construction and source of all strains used in this study (Microsoft Word, DOCX file).

Supplementary file 6. Plasmids used in this study. The table provides descriptions of all the plasmids used in this study, including details of their construction or source (Microsoft Word, DOCX file).

Supplementary file 7. Oligonucleotides used in this study. The table shows the sequences of all synthetic oligonucleotides used in this study (Microsoft Word, DOCX file).

References

Abraham, MJ, Murtola, T, Schulz, R, Páll, S, Smith, JC, Hess, B, Lindahl, E (2015). GROMACS: High performance molecular simulations through multi-level parallelism from laptops to supercomputers. *SoftwareX* **1-2**:19-25.

Anand, D, Schumacher, D, Søgaard-Andersen, L (2020). SMC and the bactofilin/PadC scaffold have distinct yet redundant functions in chromosome segregation and organization in *Myxococcus xanthus*. *Mol Microbiol* **114**:839-856.

Ausmees, N, Kuhn, JR, Jacobs-Wagner, C (2003). The bacterial cytoskeleton: an intermediate filament-like function in cell shape. *Cell* **115**:705-713.

Bailey, TL, Elkan, C (1994). Fitting a mixture model by expectation maximization to discover motifs in biopolymers. *Proc Int Conf Intell Syst Mol Biol* **2**:28-36.

Bendezu, FO, Hale, CA, Bernhardt, TG, de Boer, PA (2009). RodZ (YfgA) is required for proper assembly of the MreB actin cytoskeleton and cell shape in *E. coli*. *EMBO J* **28**:193-204.

Berendsen, HJC, Postma, JPM, van Gunsteren, WF, DiNola, A, Haak, JR (1984). Molecular dynamics with coupling to an external bath. *J Chem Phys* **81**:3684–3690.

Billini, M, Biboy, J, Kuhn, J, Vollmer, W, Thanbichler, M (2019). A specialized MreB-dependent cell wall biosynthetic complex mediates the formation of stalk-specific peptidoglycan in *Caulobacter crescentus*. *PLoS Genet* **15**:e1007897.

Brockett, MR, Lee, J, Cox, JV, Liechti, GW, Ouellette, SP (2021). A dynamic, ring-forming bactofilin critical for maintaining cell size in the obligate intracellular bacterium *Chlamydia trachomatis*. *Infect Immun* **89**:e0020321.

Bussi, G, Donadio, D, Parrinello, M (2007). Canonical sampling through velocity rescaling. *J Chem Phys* **126**:014101.

Cabeen, MT, Jacobs-Wagner, C (2010). The bacterial cytoskeleton. *Annu Rev Genet* **44**:365-392.

Caccamo, PD, Jacq, M, VanNieuwenhze, MS, Brun, YV (2020). A division of labor in the recruitment and topological organization of a bacterial morphogenic complex. *Curr Biol* **30**:3908-3922.

Chow, TC, Schmidt, JM (1974). Fatty acid composition of *Caulobacter crescentus*. *J Gen Microbiol* **83**:369-373.

Contreras, I, Shapiro, L, Henry, S (1978). Membrane phospholipid composition of *Caulobacter crescentus*. *J Bacteriol* **135**:1130-1136.

Darden, T, York, D, Pedersen, L (1993). Particle mesh Ewald: An N·log(N) method for Ewald sums in large systems. *J Chem Phys* **98**:10089–10092.

De Siervo, AJ, Homola, AD (1980). Analysis of *Caulobacter crescentus* lipids. *J Bacteriol* **143**:1215-1222.

Deng, X, Gonzalez Llamazares, A, Wagstaff, JM, Hale, VL, Cannone, G, McLaughlin, SH, Kureisaite-Ciziene, D, Löwe, J (2019). The structure of bactofilin filaments reveals their mode of membrane binding and lack of polarity. *Nat Microbiol* **4**:2357-2368.

Eddy, SR (2011). Accelerated profile HMM searches. *PLoS Comput Biol* **7**:e1002195.

Edgar, RC (2004). MUSCLE: multiple sequence alignment with high accuracy and high throughput. *Nucleic Acids Res* **32**:1792-1797.

El Andari, J, Altegoer, F, Bange, G, Graumann, PL (2015). *Bacillus subtilis* bactofilins are essential for flagellar hook- and filament assembly and dynamically localize into structures of less than 100 nm diameter underneath the cell membrane. *PLoS One* **10**:e0141546.

Ely, B (1991). Genetics of *Caulobacter crescentus*. *Methods Enzymol* **204**:372-384.

Evinger, M, Agabian, N (1977). Envelope-associated nucleoid from *Caulobacter crescentus* stalked and swarmer cells. *J Bacteriol* **132**:294-301.

Frirdich, E, Vermeulen, J, Biboy, J, Vollmer, W, Gaynor, EC (2023). Multiple *Campylobacter jejuni* proteins affecting the peptidoglycan structure and the degree of helical cell curvature. *Front Microbiol* **14**:1162806.

Guzman, LM, Belin, D, Carson, MJ, Beckwith, J (1995). Tight regulation, modulation, and high-level expression by vectors containing the arabinose P_{BAD} promoter. *J Bacteriol* **177**:4121-4130.

Hartmann, R, van Teeseling, MCF, Thanbichler, M, Drescher, K (2020). BacStalk: A comprehensive and interactive image analysis software tool for bacterial cell biology. *Mol Microbiol* **114**:140-150.

Hay, NA, Tipper, DJ, Gygi, D, Hughes, C (1999). A novel membrane protein influencing cell shape and multicellular swarming of *Proteus mirabilis*. *J Bacteriol* **181**:2008-2016.

Hirel, PH, Schmitter, MJ, Dessen, P, Fayat, G, Blanquet, S (1989). Extent of N-terminal methionine excision from *Escherichia coli* proteins is governed by the side-chain length of the penultimate amino acid. *Proc Natl Acad Sci U S A* **86**:8247-8251.

Holtrup, S, Heimerl, T, Linne, U, Altegoer, F, Noll, F, Waidner, B (2019). Biochemical characterization of the *Helicobacter pylori* bactofilin-homolog HP1542. *PLoS One* **14**:e0218474.

Huang, J, Rauscher, S, Nawrocki, G, Ran, T, Feig, M, de Groot, BL, Grubmuller, H, MacKerell, AD, Jr. (2017). CHARMM36m: an improved force field for folded and intrinsically disordered proteins. *Nat Methods* **14**:71-73.

Hughes, HV, Lisher, JP, Hardy, GG, Kysela, DT, Arnold, RJ, Giedroc, DP, Brun, YV (2013). Co-ordinate synthesis and protein localization in a bacterial organelle by the action of a penicillin-binding-protein. *Mol Microbiol* **90**:1162-1177.

Hunter, JD (2007). Matplotlib: a 2D graphics environment. *Comput Sci Eng* **9**:90-95.

Izquierdo-Martinez, A, Billini, M, Miguel-Ruano, V, Hernandez-Tamayo, R, Richter, P, Biboy, J, Batuecas, MT, Glatter, T, Vollmer, W, Graumann, PL*, et al.* (2023). DipM controls multiple autolysins and mediates a regulatory feedback loop promoting cell constriction in *Caulobacter crescentus*. *Nat Commun* **14**:4095.

Jackson, KM, Schwartz, C, Wachter, J, Rosa, PA, Stewart, PE (2018). A widely conserved bacterial cytoskeletal component influences unique helical shape and motility of the spirochete *Leptospira biflexa*. *Mol Microbiol* **108**:77-89.

Jacq, M, Caccomo, PD, Brun, YV (2024) Functional specialization of the subdomains of a bactofilin driving stalk morphogenesis in *Asticcacaulis biprosthecum*. *bioRxiv* DOI: 10.1101/2024.12.16.628611.

Jaqaman, K, Loerke, D, Mettlen, M, Kuwata, H, Grinstein, S, Schmid, SL, Danuser, G (2008). Robust single-particle tracking in live-cell time-lapse sequences. *Nat Methods* **5**:695-702.

Jo, S, Kim, T, Iyer, VG, Im, W (2008). CHARMM-GUI: a web-based graphical user interface for CHARMM. *J Comput Chem* **29**:1859-1865.

Jo, S, Lim, JB, Klauda, JB, Im, W (2009). CHARMM-GUI Membrane Builder for mixed bilayers and its application to yeast membranes. *Biophys J* **97**:50-58.

Jones, LJ, Carballido-Lopez, R, Errington, J (2001). Control of cell shape in bacteria: helical, actin-like filaments in *Bacillus subtilis*. *Cell* **104**:913-922.

Kassem, MM, Wang, Y, Boomsma, W, Lindorff-Larsen, K (2016). Structure of the bacterial cytoskeleton protein bactofilin by NMR chemical shifts and sequence variation. *Biophys J* **110**:2342-2348.

Koch, MK, McHugh, CA, Hoiczyk, E (2011). BacM, an N-terminally processed bactofilin of *Myxococcus xanthus*, is crucial for proper cell shape. *Mol Microbiol* **80**:1031-1051.

Konermann, L, Pan, J, Liu, YH (2011). Hydrogen exchange mass spectrometry for studying protein structure and dynamics. *Chem Soc Rev* **40**:1224-1234.

Kühn, J, Briegel, A, Mörschel, E, Kahnt, J, Leser, K, Wick, S, Jensen, GJ, Thanbichler, M (2010). Bactofilins, a ubiquitous class of cytoskeletal proteins mediating polar localization of a cell wall synthase in *Caulobacter crescentus*. *EMBO J* **29**:327-339.

Lee, J, Cheng, X, Swails, JM, Yeom, MS, Eastman, PK, Lemkul, JA, Wei, S, Buckner, J, Jeong, JC, Qi, Y*, et al.* (2016). CHARMM-GUI input generator for NAMD, GROMACS, AMBER, OpenMM, and CHARMM/OpenMM simulations using the CHARMM36 additive force field. *J Chem Theory Comput* **12**:405-413.

Lee, J, Cox, JV, Ouellette, SP (2023). The unique N-terminal domain of chlamydial bactofilin mediates its membrane localization and ring-forming properties. *J Bacteriol* **205**:e0009223.

Lin, L, Osorio Valeriano, M, Harms, A, Søgaard-Andersen, L, Thanbichler, M (2017). Bactofilin-mediated organization of the ParAB*S* chromosome segregation system in *Myxococcus xanthus*. *Nat Commun* **8**:1817.

Liu, Y, van den Ent, F, Löwe, J (2024). Filament structure and subcellular organization of the bacterial intermediate filament-like protein crescentin. *Proc Natl Acad Sci U S A* **121**:e2309984121.

Löwe, J, Amos, LA (1998). Crystal structure of the bacterial cell-division protein FtsZ. *Nature* **391**:203-206.

Marblestone, JG, Edavettal, SC, Lim, Y, Lim, P, Zuo, X, Butt, TR (2006). Comparison of SUMO fusion technology with traditional gene fusion systems: enhanced expression and solubility with SUMO. *Protein Sci* **15**:182-189.

McQuillen, R, Xiao, J (2020). Insights into the structure, function, and dynamics of the bacterial cytokinetic FtsZ-ring. *Annu Rev Biophys* **49**:309-341.

Mohr, CD, Jenal, U, Shapiro, L (1996). Flagellar assembly in *Caulobacter crescentus*: a basal body P-ring null mutation affects stability of the L-ring protein. *J Bacteriol* **178**:675-682.

Mukherjee, A, Dai, K, Lutkenhaus, J (1993). *Escherichia coli* cell division protein FtsZ is a guanine nucleotide binding protein. *Proc Natl Acad Sci U S A* **90**:1053-1057.

Oviedo-Bocanegra, LM, Hinrichs, R, Rotter, DAO, Dersch, S, Graumann, PL (2021). Single molecule/particle tracking analysis program SMTracker 2.0 reveals different dynamics of proteins within the RNA degrado-some complex in *Bacillus subtilis*. *Nucleic Acids Res* **49**:e112.

Páll, S, Hess, B (2013). A flexible algorithm for calculating pair interactions on SIMD architectures. *Comput Phys Commun* **184**:2641-2650.

Paysan-Lafosse, T, Blum, M, Chuguransky, S, Grego, T, Pinto, BL, Salazar, GA, Bileschi, ML, Bork, P, Bridge, A, Colwell, L*, et al.* (2022). InterPro in 2022. *Nucleic Acids Res* **51**:D418-D427.

Pichoff, S, Lutkenhaus, J (2005). Tethering the Z ring to the membrane through a conserved membrane targeting sequence in FtsA. *Mol Microbiol* **55**:1722-1734.

1095 Plank, M, Wadhams, GH, Leake, MC (2009). Millisecond timescale slimfield imaging and automated
1096 quantification of single fluorescent protein molecules for use in probing complex biological processes.
1097 *Integr Biol (Camb)* **1**:602-612.

1098 Pöhl, S, Osorio-Valeriano, M, Cserti, E, Harberding, J, Hernandez-Tamayo, R, Biboy, J, Sobetzko, P, Vollmer,
1099 W, Graumann, PL, Thanbichler, M (2024). A dynamic bactofilin cytoskeleton cooperates with an M23
1100 endopeptidase to control bacterial morphogenesis. *Elife* **12**:RP86577.

1101 Poindexter, JS (1964). Biological properties and classification of the *Caulobacter* group. *Bacteriol Rev*
1102 **28**:231-295.

1103 Richter, P, Melzer, B, Müller, FD (2023). Interacting bactofilins impact cell shape of the MreB-less
1104 multicellular *Rhodomicrobium vannielii*. *PLoS Genet* **19**:e1010788.

1105 Rohs, PDA, Bernhardt, TG (2021). Growth and Division of the peptidoglycan matrix. *Annu Rev Microbiol*
1106 **75**:315-336.

1107 Salje, J, van den Ent, F, de Boer, P, Löwe, J (2011). Direct membrane binding by bacterial actin MreB. *Mol*
1108 *Cell* **43**:478-487.

1109 Sapay, N, Guermeur, Y, Deleage, G (2006). Prediction of amphipathic in-plane membrane anchors in
1110 monotopic proteins using a SVM classifier. *BMC Bioinformatics* **7**:255.

1111 Schindelin, J, Arganda-Carreras, I, Frise, E, Kaynig, V, Longair, M, Pietzsch, T, Preibisch, S, Rueden, C,
1112 Saalfeld, S, Schmid, B*, et al.* (2012). Fiji: an open-source platform for biological-image analysis. *Nat*
1113 *Methods* **9**:676-682.

1114 Schmidt, J. (1968) Stalk elongation in mutants of *Caulobacter crescentus*. *J Gen Microbiol* **53**:291-298.

1115 Shi, C, Fricke, P, Lin, L, Chevelkov, V, Wegstroth, M, Giller, K, Becker, S, Thanbichler, M, Lange, A (2015).
1116 Atomic-resolution structure of cytoskeletal bactofilin by solid-state NMR. *Sci Adv* **1**:e1501087.

1117 Sichel, SR, Bratton, BP, Salama, NR (2022). Distinct regions of *H. pylori*'s bactofilin CcmA regulate protein-
1118 protein interactions to control helical cell shape. *Elife* **11**:e80111.

1119 Stankeviciute, G, Guan, Z, Goldfine, H, Klein, EA (2019). *Caulobacter crescentus* adapts to phosphate
1120 starvation by synthesizing anionic glycoglycerolipids and a novel glycosphingolipid. *mBio* **10**:e00107-
1121 00119.

1122 Strobel, W, Möll, A, Kiekebusch, D, Klein, KE, Thanbichler, M (2014) Function and localization dynamics of
1123 bifunctional penicillin-binding proteins in *Caulobacter crescentus*. *J Bacteriol* **196**:1627-1639.

1124 Sycuro, LK, Pincus, Z, Gutierrez, KD, Biboy, J, Stern, CA, Vollmer, W, Salama, NR (2010). Peptidoglycan
1125 crosslinking relaxation promotes *Helicobacter pylori*'s helical shape and stomach colonization. *Cell*
1126 **141**:822-833.

1127 Thanbichler, M, Iniesta, AA, Shapiro, L (2007). A comprehensive set of plasmids for vanillate- and xylose-
1128 inducible gene expression in *Caulobacter crescentus*. *Nucleic Acids Res* **35**:e137.

1129 Thanbichler, M, Shapiro, L (2006). MipZ, a spatial regulator coordinating chromosome segregation with
1130 cell division in *Caulobacter*. *Cell* **126**:147-162.

1131 UniProt Consortium (2023). UniProt: the Universal Protein Knowledgebase in 2023. *Nucleic Acids Res*
1132 **51**:D523-D531.

1133 van den Ent, F, Amos, LA, Löwe, J (2001). Prokaryotic origin of the actin cytoskeleton. *Nature* **413**:39-44.

Vasa, S, Lin, L, Shi, C, Habenstein, B, Riedel, D, Kühn, J, Thanbichler, M, Lange, A (2015). β-Helical architecture of cytoskeletal bactofilin filaments revealed by solid-state NMR. *Proc Natl Acad Sci U S A* **112**:E127-136.

Wagstaff, J, Löwe, J (2018). Prokaryotic cytoskeletons: protein filaments organizing small cells. *Nat Rev Microbiol* **16**:187-201.

Wales, TE, Fadgen, KE, Gerhardt, GC, Engen, JR (2008). High-speed and high-resolution UPLC separation at zero degrees Celsius. *Anal Chem* **80**:6815-6820.

Waskom, ML (2021). seaborn: statistical data visualization. *J Open Source Softw* **6**:3021.

Waterhouse, AM, Procter, JB, Martin, DM, Clamp, M, Barton, GJ (2009). Jalview Version 2 – a multiple sequence alignment editor and analysis workbench. *Bioinformatics* **25**:1189-1191.

Wolfenden, R, Andersson, L, Cullis, PM, Southgate, CC (1981). Affinities of amino acid side chains for solvent water. *Biochemistry* **20**:849-855.

Wu, EL, Cheng, X, Jo, S, Rui, H, Song, KC, Davila-Contreras, EM, Qi, Y, Lee, J, Monje-Galvan, V, Venable, RM*, et al.* (2014). CHARMM-GUI Membrane Builder toward realistic biological membrane simulations. *J Comput Chem* **35**:1997-2004.

Yakhnina, AA, Gitai Z (2013) Diverse functions for six glycosyltransferases in *Caulobacter crescentus* cell wall assembly. *J Bacteriol* **195**:4527-4535.

Zuckerman, DM, Boucher, LE, Xie, K, Engelhardt, H, Bosch, J, Hoiczyk, E (2015). The bactofilin cytoskeleton protein BacM of *Myxococcus xanthus* forms an extended β-sheet structure likely mediated by hydrophobic interactions. *PLoS One* **10**:e0121074.

Figures

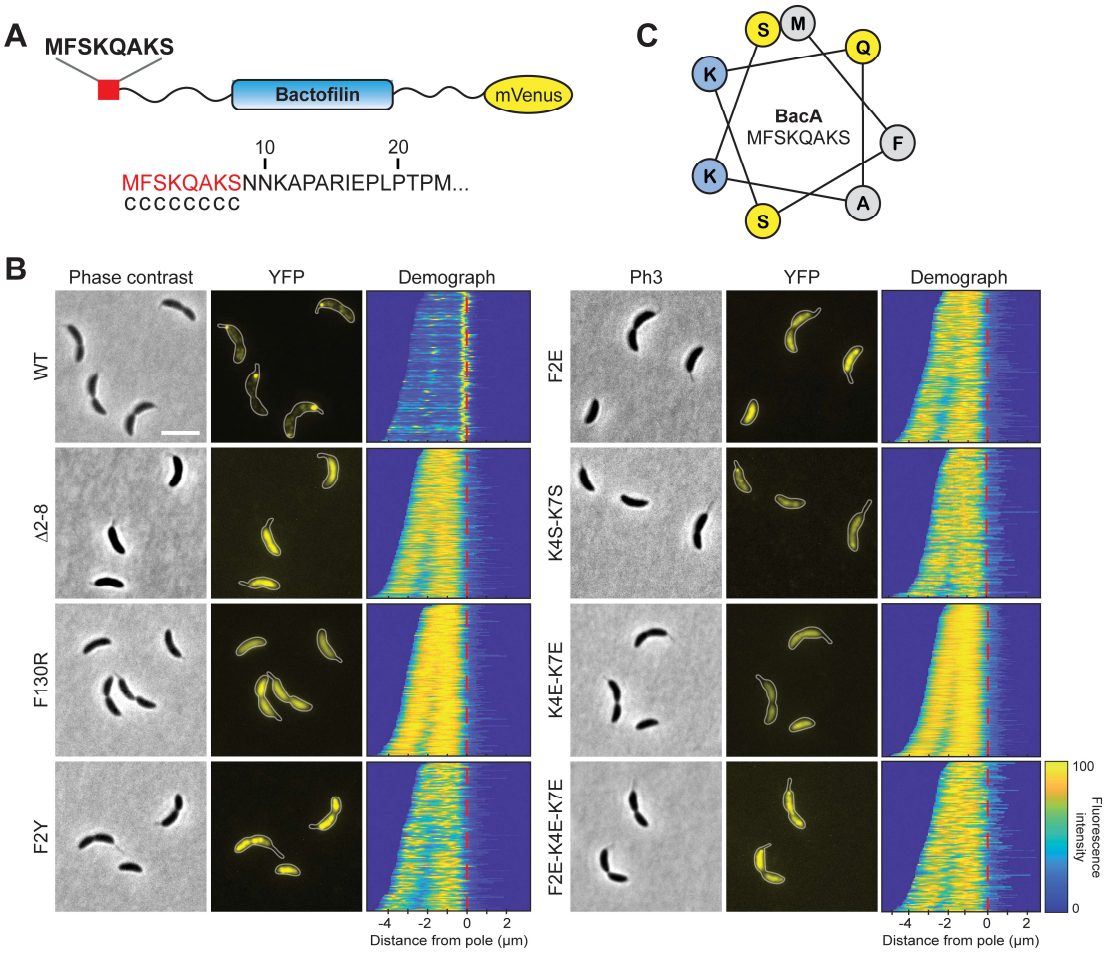

Figure 3. Identification of residues critical for the membrane-binding activity of BacA *in vivo*. (A) Schematic representation of the BacA-mVenus fusion protein used in this study. The proposed membrane-targeting sequence is highlighted in red. The sequence at the bottom shows that result of an amphipathic helix prediction for BacA using the AMPHIPASEEK software (Sapay et al., 2006). Residues predicted to be located in an unstructured, randomly coiled region are labeled with "c". **(B)** Localization patterns of mutant BacA-mVenus variants. Δ*bacAB* cells producing BacA-mVenus or mutant variants thereof (strains LY84, LY89, LY90, LY97, LY111, LY112, LY113, LY119) were analyzed by phase contrast and fluorescence microscopy. The outlines of the cells are shown in the fluorescence images. Demographs summarizing the single-cell fluorescence profiles obtained from random sub-populations of cells are given next to the respective fluorescence images. The numbers of cells analyzed are: WT (130), Δ2-8 (292), F130R (156), F2Y (138), F2E (194), K4S-K7S (151), K4E-K7E (382), F2E-K4E-K7E (130). The vertical red line indicates the junction between cell body and the stalk. Scale bar: 2 µm. **(C)** Helical wheel diagram of the first eight amino acids of BacA. Residues are colored by properties: hydrophobic (gray), basic (blue), uncharged (yellow).

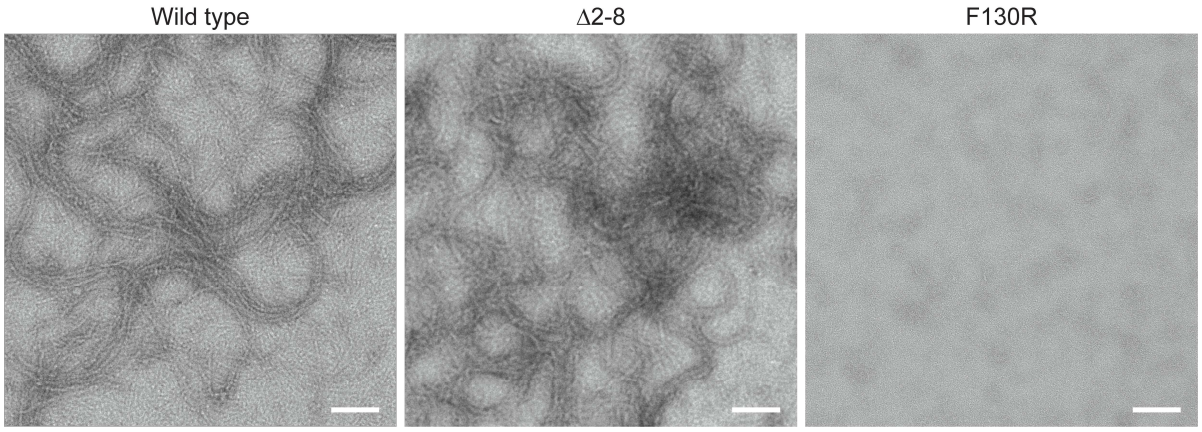

Figure 1–figure supplement 1. Ultrastructure of different BacA variants. Wild-type BacA, its MTS-free Δ2-8 variant and its polymerization-deficient F130R variant (xx mg/ml) were stained with uranyl acetate and visualized by transmission electron microscopy. Bar: 100 nm.

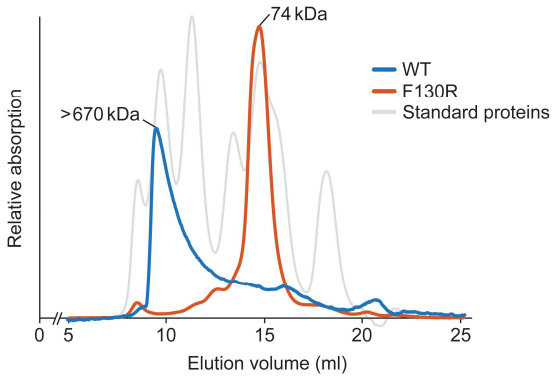

Figure 1–figure supplement 2. Size-exclusion chromatography analysis of wild-type BacA and its F130R variant. The indicated proteins were applied to a Superdex 200 size-exclusion column and detected photometrically at a wavelength of 280 nm. The following standard proteins were analyzed as a reference to calibrate the column: Thyroglobulin (669 kDa), Ferritin (440 kDa), Aldolase (158 kDa), Conalbumin (75 kDa), Ovalbumin (44 kDa), Ribonuclease A (14 kDa).

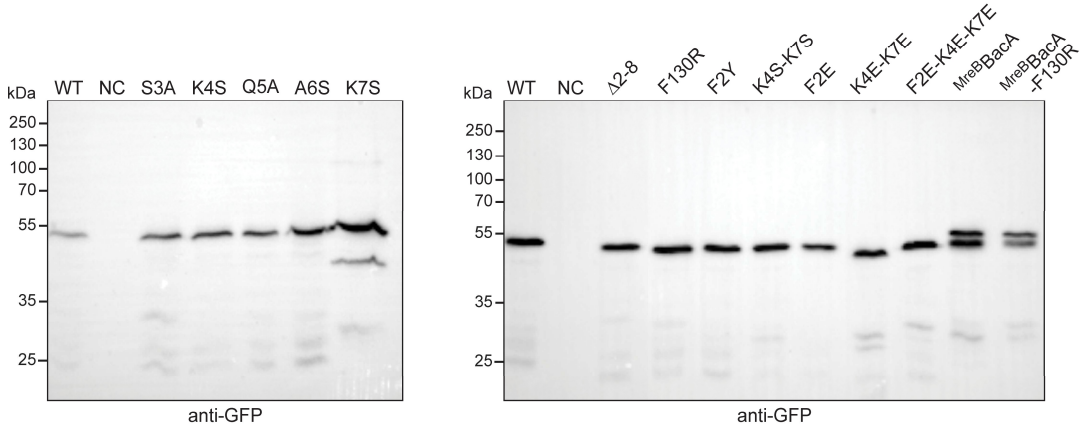

Figure 1–figure supplement 3. Stability of different BacA-mVenus variants. Derivates of strain JK5 (Δ*bacAB*) carrying the indicated alleles of *bacA-mVenus* under the control of the xylose-inducible P_{xyl} promoter were grown overnight, diluted to an OD_{600} of ~ 0.1 and incubated for another hour. The strains were then induced with 0.03% xylose for 1 h and subjected to immunoblot analysis with an anti-GFP antibody. Strain JK5 was analyzed as a negative control (NC). The positions of standard proteins (in kDa) are indicated on the left side of the images.

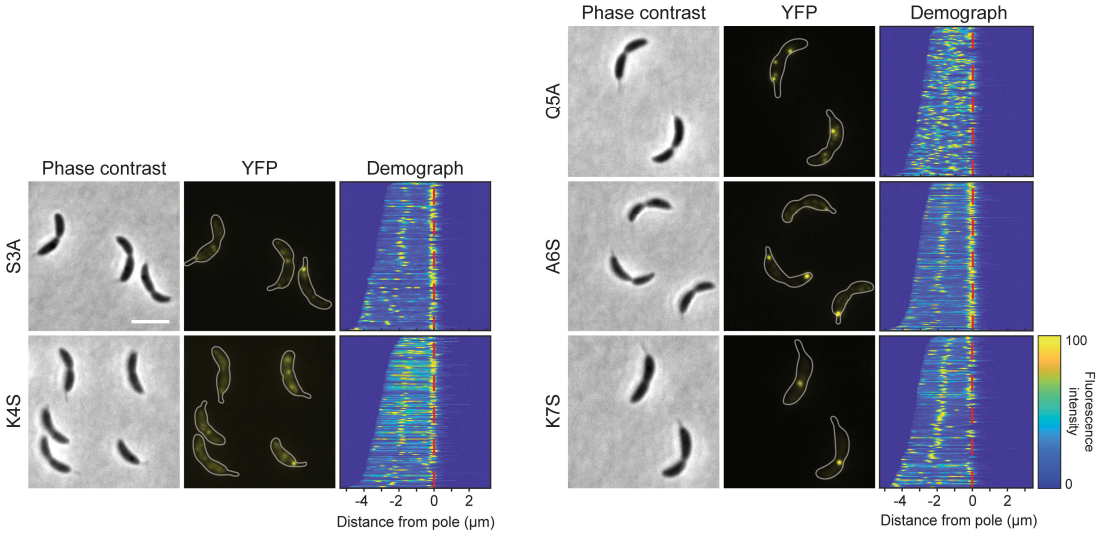

Figure 1–figure supplement 4. Localization patterns of different BacA-mVenus variants. Δ*bacAB* cells producing the indicated BacA-mVenus variants (strains LY95, LY88, LY96, LY91, LY92) were analyzed by phase contrast and fluorescence microscopy. The outlines of the cells are shown in the fluorescence images. Demographs summarizing the single-cell fluorescence profiles obtained from random subpopulations of cells are given next to the respective fluorescence images. The numbers of cells analyzed are: S3A (109), K4S (150), Q5A (121), A6S (184), K7S (128). The vertical red line indicates the junction between cell body and the stalk. Scale bar: 2 µm.

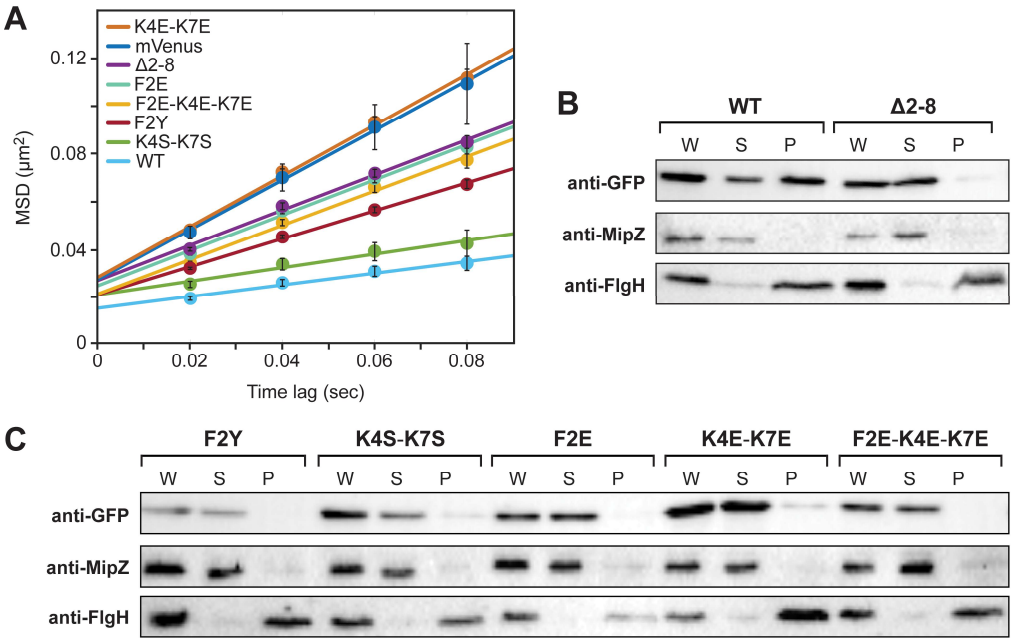

Figure 4. Verification of residues M1, F2 and K4/K7 as critical components of the BacA MTS. (A) Mobility of the indicated BacA-mVenus fusion proteins. Shown is the average mean-squared displacement (MSD) (± SD) as a function of time, based on single-particle tracking analysis. The fitted lines were obtained by linear regression analysis. **(B)** Cell fractionation experiment investigating the membrane-binding activity of BacA-mVenus (WT) or a mutant variant lacking the predicted MTS (Δ2-8). Whole-cell lysates (W) as well as the soluble (S) and pellet (P) fractions of cells producing the indicated proteins were subjected to immunoblot analysis with an anti-GFP antibody, detecting the BacA-mVenus fusion protein. As controls, the same samples were probed with antibodies raised against the soluble cell division regulator MipZ (Thanbichler and Shapiro, 2006) or the membrane-bound flagellar L-ring subunit FlgH (Mohr et al., 1996) from *C. crescentus*. **(C)** As in panel B, but for cells producing mutant BacA-mVenus variants with single or multiple amino-acid exchanges in the predicted MTS. Shown are representative images (n=3 independent replicates). The strains used are given in the legend to Figure 1B.

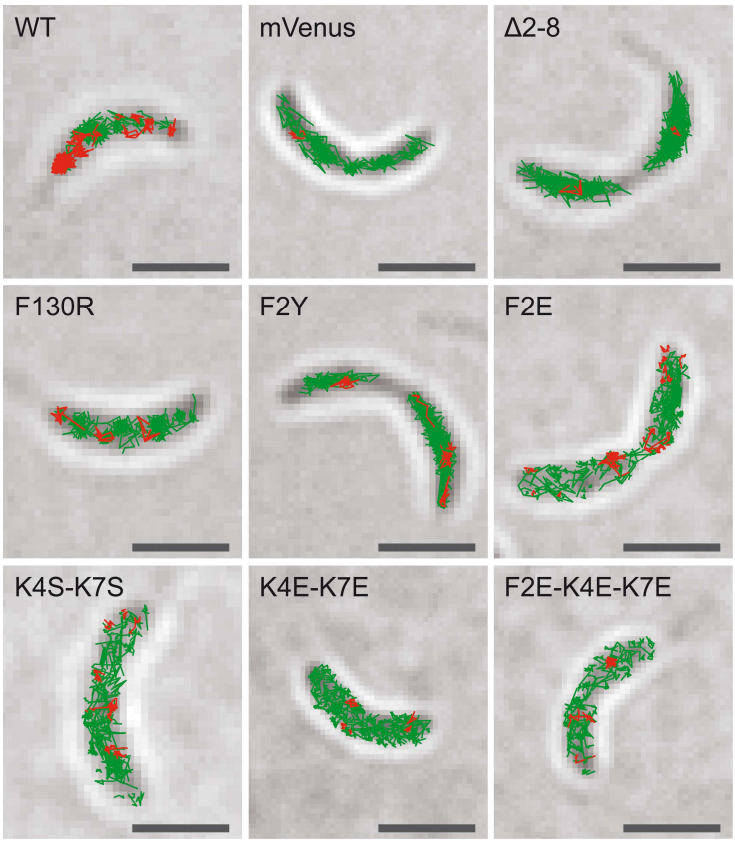

Figure 2–figure supplement 1. Subcellular localization of the single-molecule tracks obtained for different BacA-mVenus variants. The single-particle tracks determined for wild-type BacA-mVenus, free mVenus and the indicated BacA-mVenus variants were mapped onto phase contrast images of the cells in which they were recorded. The images show the results obtained from representative cells. Red lines indicate slow-moving particles, green lines indicate fast-moving particles (as defined in **Supplementary file 1**). Bar: 1 µm.

Figure 2–video 1. Single-particle dynamics of different BacA-mVenus variants. The movies show the single-particle dynamics of wild-type BacA-mVenus, free mVenus and the indicated BacA-mVenus variants in representative cells. The outlines of the cells are indicated in white. Red lines show the tracks of individual particles. Images were acquired at 20-ms intervals. Bar: 1 µm.

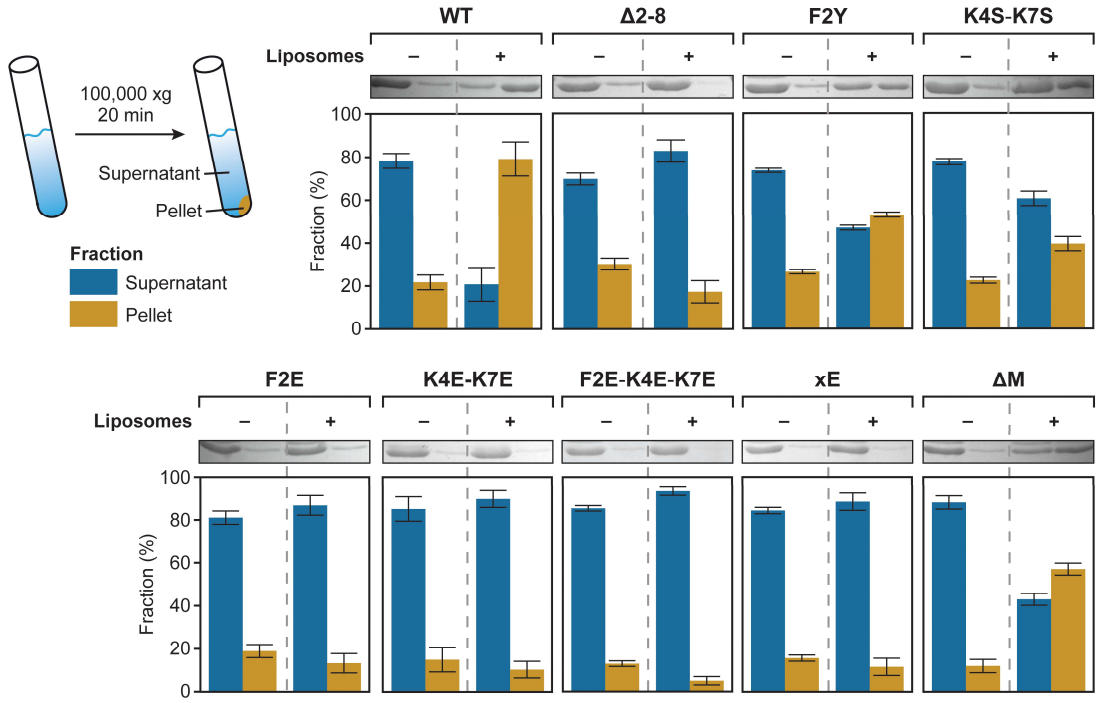

Figure 3. Co-sedimentation analysis of the association of various BacA variants with liposomes. The indicated proteins (20 µM) were incubated without (-) or with (+) liposomes (0.4 mg/mL) prior to ultracentrifugation. The supernatant and pellet fractions of each mixture were analyzed by SDS gel electrophoresis. Shown are scans of representative gels and a quantification of the average relative signal intensities (± SD) obtained for the different fractions (n=3 independent replicates).

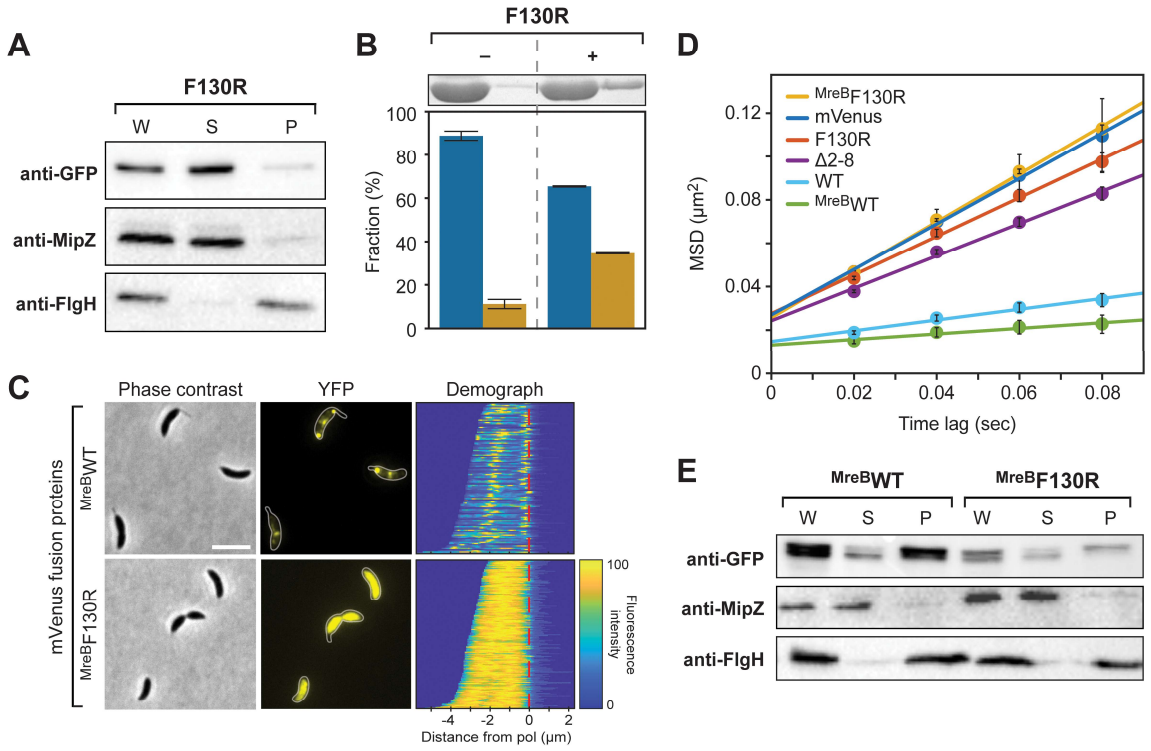

Figure 4. Interplay between BacA assembly and membrane binding. (A) Cell fractionation experiment investigating the membrane-binding activity of the polymerization-deficient F130R variant of BacA-mVenus *in vivo* (LY119). The analysis was performed as described for **Figure 2B**. **(B)** Co-sedimentation analysis of the association of BacA-F130R with liposomes *in vitro*, performed as described for **Figure 3**. **(C)** Role of polymerization in the membrane association of a BacA-mVenus variant carrying the membrane-targeting sequence of *E. coli* MreB. Shown are phase contrast and fluorescence images of Δ*bacAB* mutants (LY103, LY123) producing either a BacA-mVenus variant in which the MTS is replaced by two tandem copies of the N-terminal amphiphilic helix of *E. coli* MreB (^{MreB}WT) or a polymerization-deficient variant thereof (^{MreB}F130R). Demographs summarizing the single-cell fluorescence profiles obtained from random subpopulations of cells are given next to the respective fluorescence images. The numbers of cells analyzed are: ^{MreB}WT (126), ^{MreB}F130R (169). The vertical red line indicates the junction between cell body and the stalk. Scale bar: 2 µm. **(D)** Mobility of the indicated BacA-mVenus fusion proteins. Shown is the average mean-squared displacement (MSD) (± SD) as a function of time, based on single-particle tracking analysis. The mVenus, Δ2-8 and WT data are taken from **Figure 2A** and shown for comparison. **(E)** Cell fractionation experiment investigating the membrane-binding activity of ^{MreB}BacA-mVenus (^{MreB}WT) and its polymerization-deficient F130R variant (^{MreB}F130R) *in vivo* (LY103, LY123). The analysis was performed as described for **Figure 2B.**

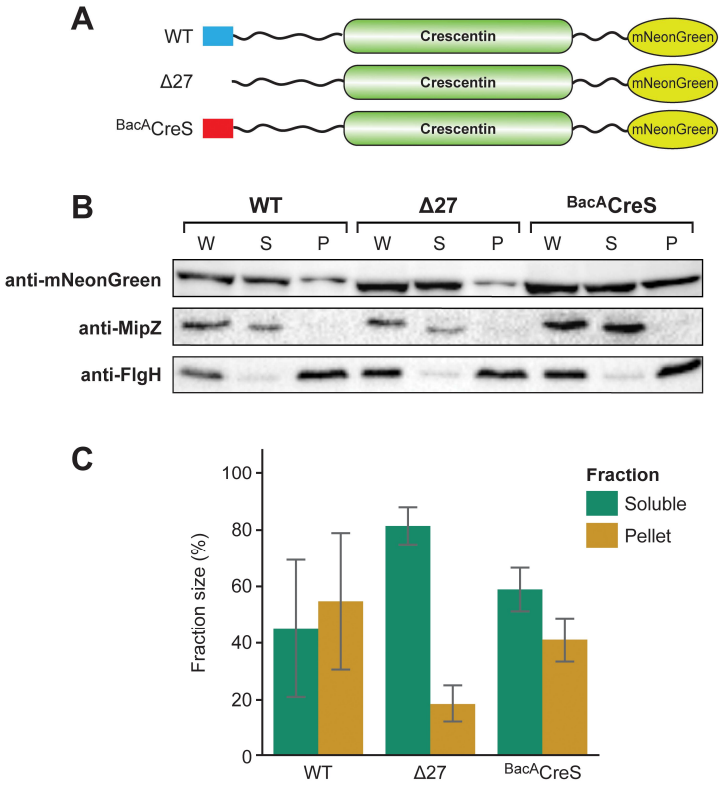

Figure 4–figure supplement 1. Solubility of different CreS-mNeonGreen variants. (A) Schematics showing the CreS-mNeonGreen variants analyzed in this study. The membrane-targeting regions of CreS and BacA are shown in blue and red, respectively. **(B)** Cell fractionation experiment investigating the membrane-binding activity of CreS-mNeonGreen (WT) or mutant variants lacking the predicted membrane-targeting region (Δ27) or containing the BacA MTS instead of the native membrane-targeting region (^{BacA}CreS). Whole-cell lysates (W) as well as the soluble (S) and pellet (P) fractions of cells producing the indicated proteins were subjected to immunoblot analysis with an anti-mNeonGreen antibody. As controls, the same samples were probed with antibodies raised against the soluble cell division regulator MipZ (Thanbichler and Shapiro, 2006) or the membrane-bound flagellar L-ring subunit FlgH (Mohr et al., 1996) from *C. crescentus*. Shown are representative images (n=3 independent replicates). **(C)** Quantification of the relative amounts of CreS-mNeonGreen or its mutant variants in the soluble and pellet fractions. The intensities of the signals obtained for the soluble and pellet fractions in the analysis described in panel B were quantified and normalized to the total intensity in these two fractions. Data represent the average (± SD) of three independent replicates.

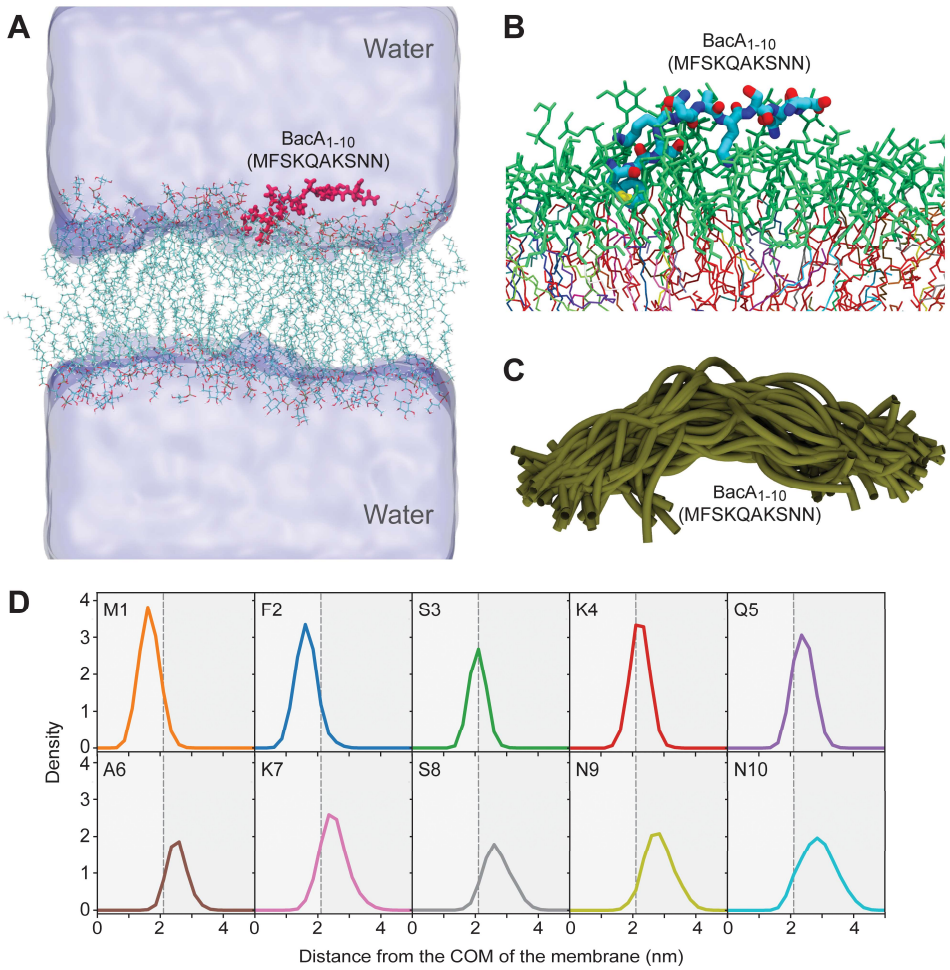

Figure 5. Molecular dynamics simulation of the interaction between the BacA MTS and a model membrane. (A) Snapshot of the molecular dynamics (MD) simulation system showing the 10-mer peptide MFSKQAKSNN ($BacA_{1-10}$; red) after binding to the lipid bilayer. The water is shown in surface representation. K^+ and Cl^- counterions are not shown. **(B)** Close-up view of a representative snapshot from the MD simulation visualizing the binding mode of the peptide on the membrane surface. **(C)** Structural overlay of 40 snapshots from the MD simulation, taken after constant time intervals from the trajectory. **(D)** Density profiles of individual residues in the wild-type peptide along the membrane normal, i.e. the z-component of the distance vector from the center-of-mass (COM) of the bilayer, with the membrane midplane located at zero. The vertical dashed black line indicates the maximum of the density distribution of the lipid headgroup phosphates.

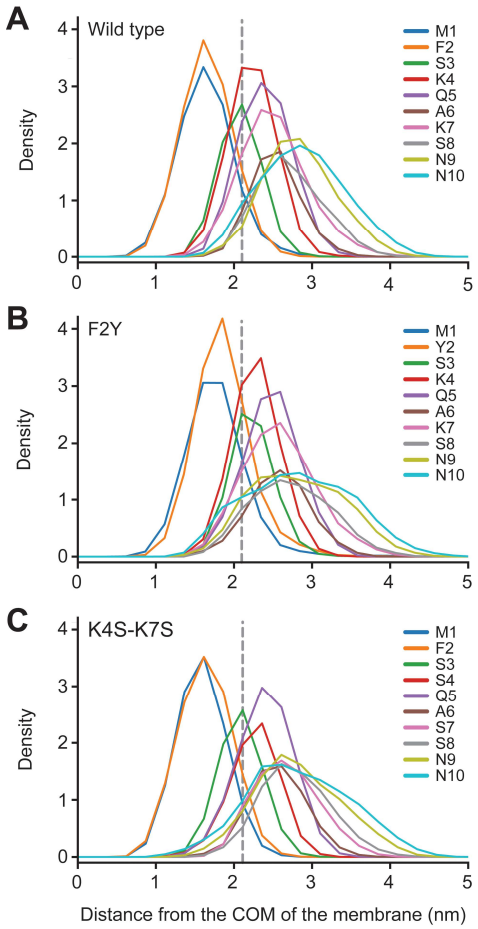

Figure 5–figure supplement 1. Density profiles for different MTS variants determined by molecular dynamics simulation. Density profiles of individual residues in the **(A)** wild-type, **(B)** F2Y and **(C)** K4S-K7S peptides along the membrane normal. The vertical dashed black line indicates the maximum of the density distribution of the lipid headgroup phosphates. The data shown in panel A are reproduced from **Figure 5D** for comparison.

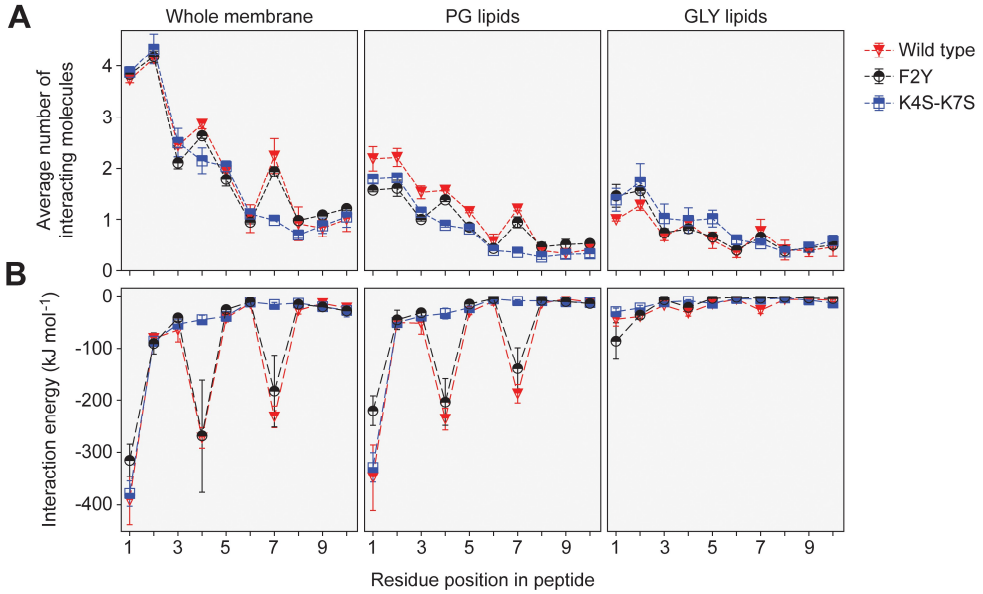

Figure 6. Contact numbers and interaction energies for different peptide-lipid bilayer interactions. (A) The graph shows the total number of contacts between individual residues in the wild-type, K4S-K7S and F2Y peptides and the lipid bilayer as well as the number of contacts with PG lipids and GLY lipids. A contact between a peptide residue and a lipid was defined to exist if any two non-hydrogen atoms of the residue and a lipid molecule were within a distance of 0.5 nm to each other. Contacts were counted for each frame of the MD trajectories and averaged. Multiple contacts between a peptide and a lipid molecule were treated as a single contact, so that the number of contacts counted was either 1 or 0. The statistical errors plotted were obtained from the difference between the two different sets of 500-ns simulations, starting with peptides in an unfolded or α-helical conformation, respectively. **(B)** Energies of the interactions between individual residues in the wild-type, K4S-K7S and F2Y peptides and the lipid bilayer. The interaction energies plotted are the combined interaction energies of all Coulomb and van-der-Waals interactions in the force field averaged over the simulation trajectories.

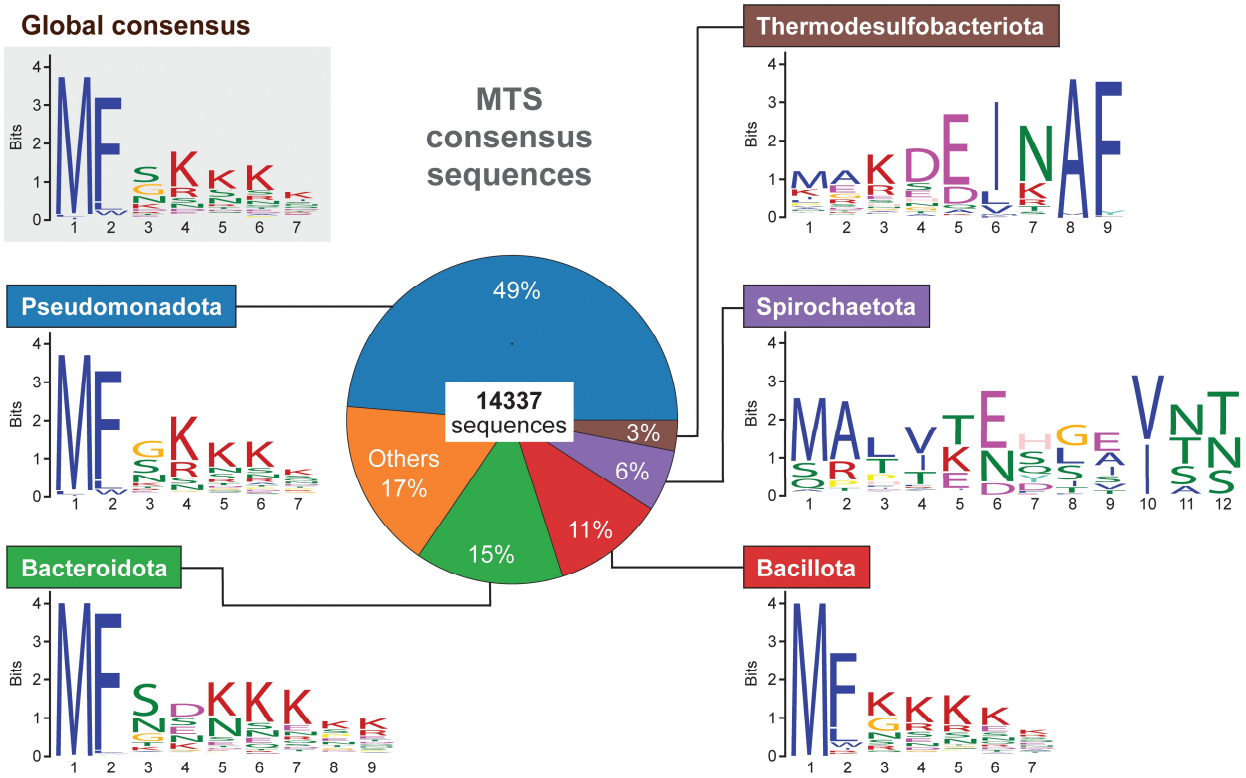

Figure 7. Conservation of the N-terminal regions of bactofilin homologs in different bacterial phyla. The pie chart in the middle shows the relative distribution of the 14337 unique bactofilin homologs analyzed among the indicated bacterial phyla. The sequence logos give the most widespread N-terminal motifs obtained either by a global analysis of all 14337 bactofilin sequences (global consensus) or by an analysis of subsets of these sequences from specific phyla.

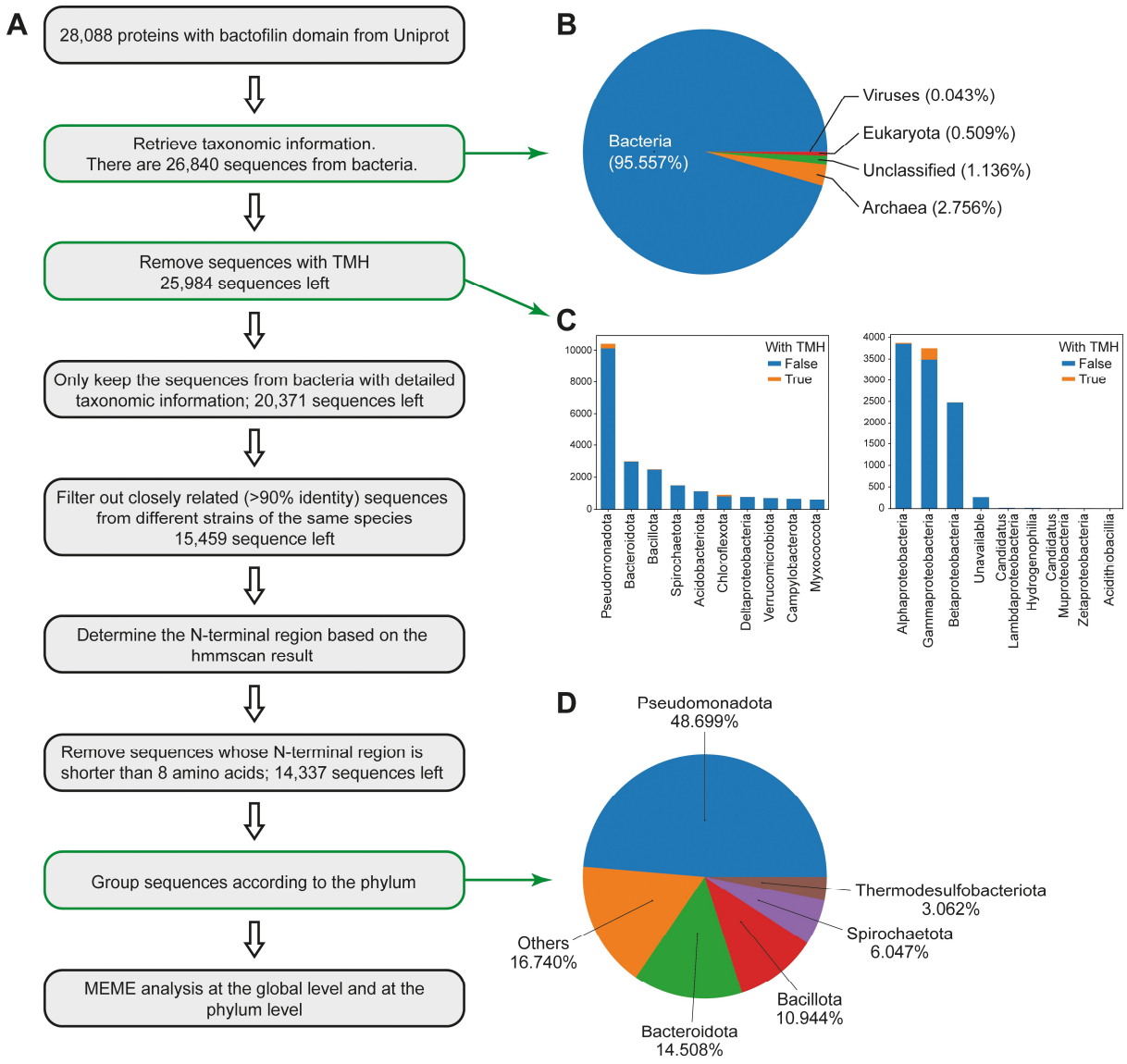

Figure 7–figure supplement 1. Assessment of the conservation of the bactofilin membrane-targeting sequence. (A) Analysis pipeline used to analyze the conservation of the N-terminal regions among bacterial bactofilin homologs. **(B)** Relative abundance of annotated bactofilin homologs in the different domains of life. **(C)** Abundance of bactofilins with predicted transmembrane helices in different bacterial lineages. **(D)** Distribution of bactofilin homologs without predicted transmembrane helices among different bacterial phyla. Small phyla contributing less than three percent of the total number of sequences have been aggregated in the category 'Others'.

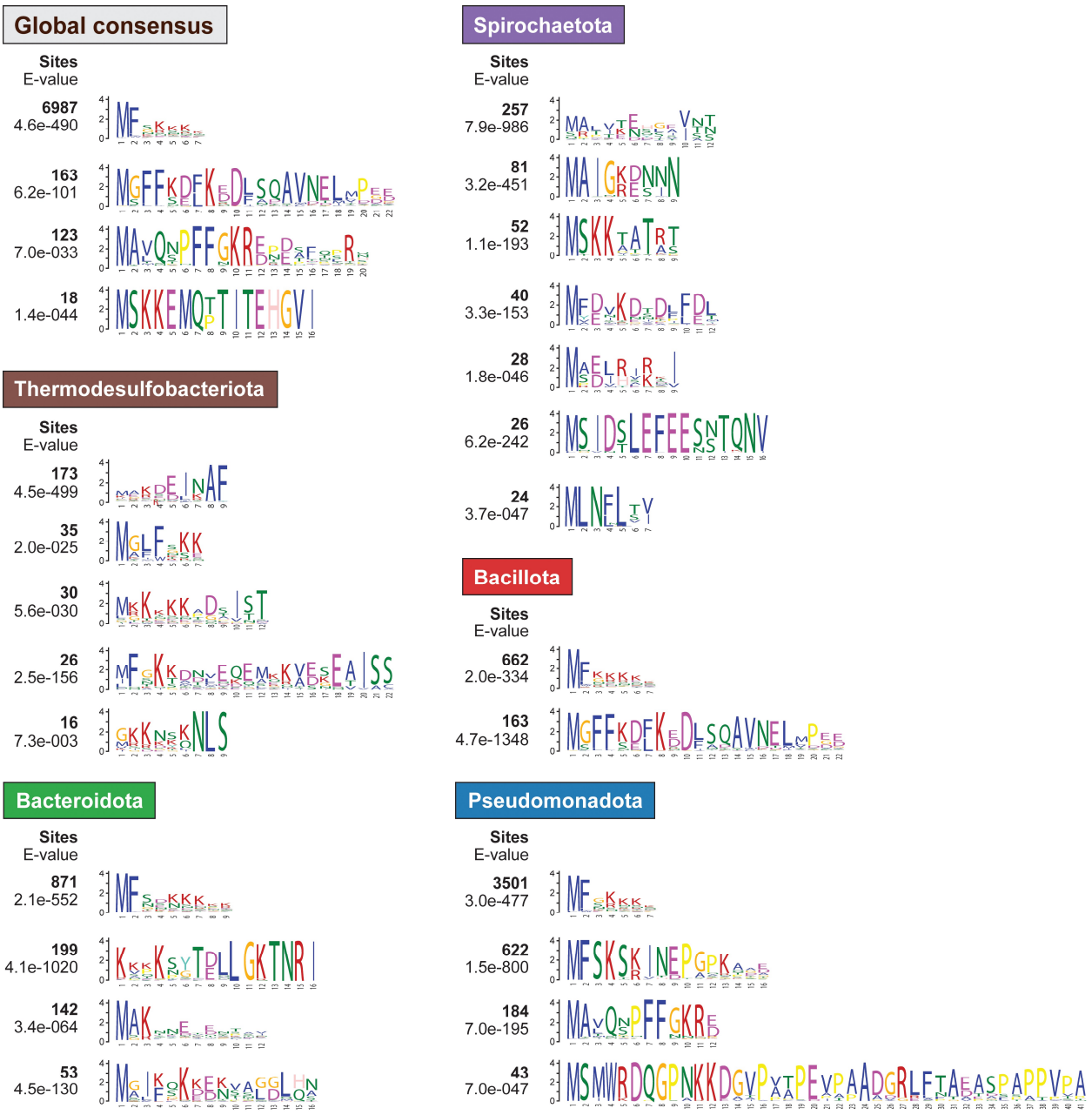

Figure 7–figure supplement 2. Conserved N-terminal motifs in bactofilin homologs from different phyla. The sequence logos give the most frequent N-terminal motifs obtained either by a global analysis of all 14,337 bactofilin sequences (global consensus) or by an analysis of subsets of these sequences from specific phyla. The number of bactofilin homologs that show N-terminal sequences corresponding to a specific motif and the likelihood for the existence of this motif are indicated on the left side of each sequence logo.

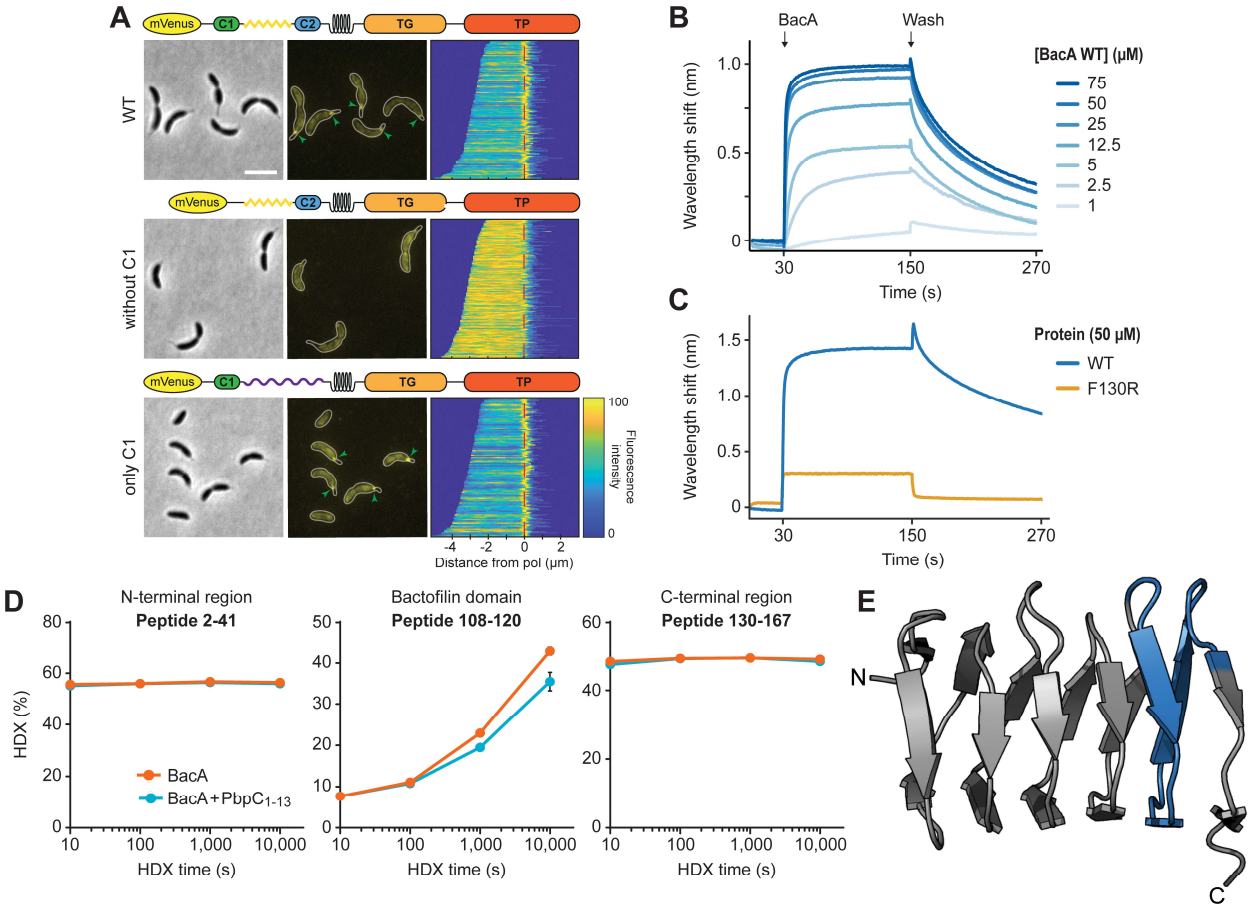

Figure 8. Interaction of BacA with its client protein PbpC. (A) Localization patterns of different PbpC variants. Δ*bacB* Δ*pbpC* cells producing mVenus-PbpC (LY75) or mutant variants thereof lacking region C1 (LY76) or carrying an unstructured region from *C. crescentus* DipM in place of the unstructured region connecting region C1 and the transmembrane helix (LY77) were analyzed by phase contrast and fluorescence microscopy. The outlines of the cells are shown in the fluorescence images. Demographs summarizing the single-cell fluorescence profiles obtained from random subpopulations of cells are given next to the respective fluorescence images. The numbers of cells analyzed are: LY75 (158), LY76 (253), LY77 (119). Scale bar: 2 µm. **(B)** Biolayer interferometric analysis of the interaction between $PbpC_{1\text{-}13aa}$ and BacA. A synthetic peptide comprising the first 13 amino acids of PbpC ($PbpC_{1\text{-}13}$) was immobilized on a biosensor and probed with increasing concentrations of BacA. After the association step, the sensor was transferred to a protein-free buffer to monitor the dissociation reaction. The graph shows a representative titration series (n=3 independent replicates). **(C)** Comparison of the interaction of $PbpC_{aa1\text{-}13}$ with BacA and its polymerization deficient F130R variant, performed as described in panel B. **(D)** Mapping of the PbpC binding site on BacA by hydrogen-deuterium exchange (HDX) mass spectrometry. The plots show the extent of deuterium uptake by three representative peptides obtained after peptic digestion of BacA protein (2.5 µM) that had been incubated in the absence or presence of the $PbpC_{1\text{-}13}$ peptide (10 µM) for the indicated time periods (see **Supplementary file 4** for the full set of peptides). **(E)** Mapping of the differences in deuterium uptake observed at t=1000 s onto the solid-state NMR structure of BacA (Shi et al., 2015).

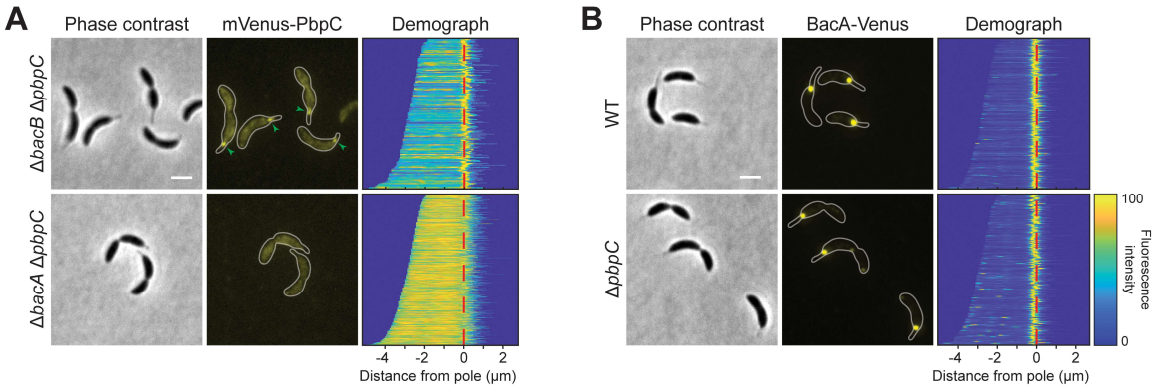

Figure 8–figure supplement 1. Localization patterns of mVenus-PbpC and BacA-Venus in different strain backgrounds. (A) Localization of mVenus-PbpC in the Δ*bacB* Δ*pbpC* (LY75) and the Δ*bacA* Δ*pbpC* (LY72) backgrounds. **(B)** Localization of BacA-Venus in the wild-type (MT256) and Δ*pbpC* (JK136) backgrounds. Cells were analyzed by phase contrast and fluorescence microscopy. The outlines of the cells are shown in the fluorescence images. Demographs summarizing the single-cell fluorescence profiles obtained from random subpopulations of cells are given next to the respective fluorescence images. The numbers of cells analyzed are: LY75 (158), LY72 (697), MT256 (264), JK136 (222). Scale bar: 1 μm.

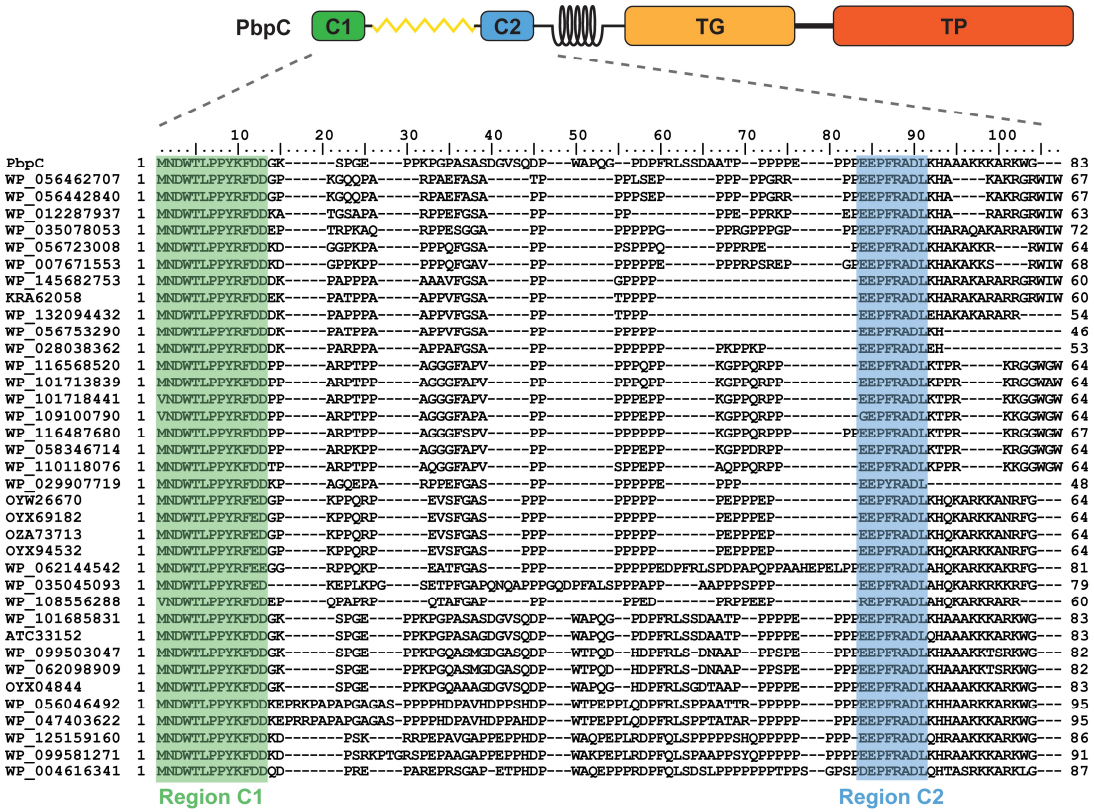

Figure 8–figure supplement 2. Sequence alignment of the cytoplasmic tail of PbpC homologs. The schematic at the top shows the structure of PbpC. Conserved domains are shown in different colors. The cytoplasmic tail of PbpC comprises conserved Region C1 (aa 1-13), a proline-rich region (aa 14-62), conserved Region C2 (aa 63-70), and a region rich in positively charged amino acids (aa 71-83), located adjacent to the transmembrane helix. Abbreviations: TG: transglycosylase domain, TP: transpeptidase domain. The NCBI identifiers of the proteins analyzed are given on the left.

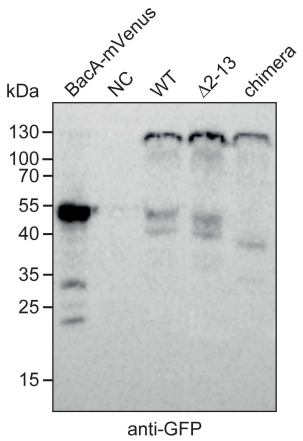

Figure 8–figure supplement 3. Stability of the mVenus-PbpC fusion proteins used in this study. Δ*bacB* Δ*pbpC* cells producing wild-type mVenus-PbpC (WT; LY75), an mVenus-PbpC variant lacking the conserved region C1 (Δ2-13; LY76) or an mVenus-PbpC variant containing an unstructured region from *C. crescentus* DipM in place of the unstructured region in between regions C1 and C2 (chimera; LY77) were grown overnight, diluted to an OD_{600} of ~0.1 and incubated for another hour. Subsequently, the cells were induced for 1.5 h with 0.3 % xylose and subjected to immunoblot analysis with an anti-GFP antibody. A Δ*bacAB* mutant producing BacA-mVenus and the wild-type strain CB15N (NC) were analyzed as positive and negative controls, respectively. The positions of standard proteins (in kDa) are indicated on the left of image.

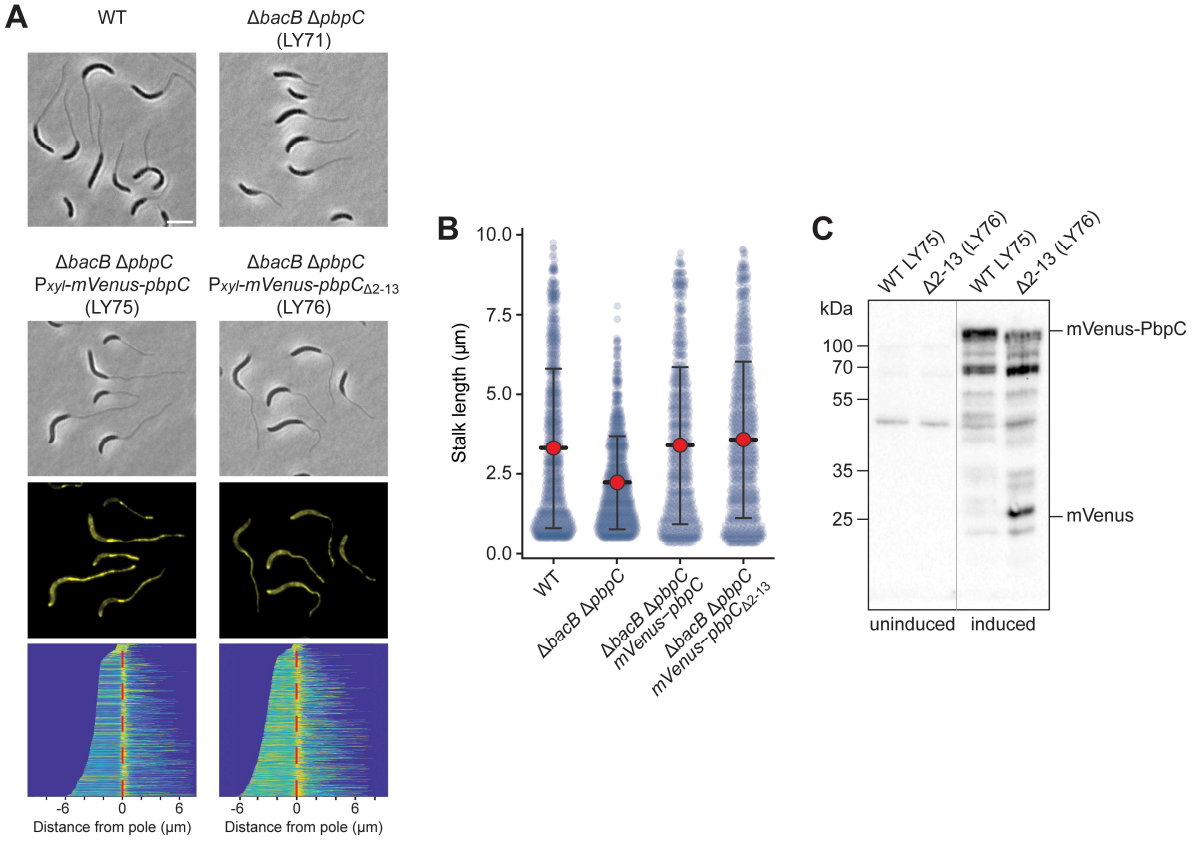

Figure 8–figure supplement 4. Relevance of BacA binding for the localization and functionality of PbpC under phosphate-limiting conditions. (A) Phase contrast and fluorescence images of the *C. crescentus* wild-type (WT), a Δ*bacB* Δ*pbpC* mutant (LY71) and a Δ*bacB* Δ*pbpC* mutant producing either mVenus-PbpC (LY75) or an N-terminally truncated variant thereof lacking region C1 (Δ2-13; LY76) under the control of a xylose-inducible promoter after 24 h of cultivation in phosphate-limited ($M2G^{-P}$) medium containing 0.3% xylose. The demographs at the bottom show the fluorescence profiles of a representative subpopulation of cells stacked on top of each other and sorted according to cell length. The numbers of cells analyzed are: 428 (WT), 415 (LY71), 659 (LY75), 753 (LY76). Bar: 3 µm. **(B)** Quantification of stalk lengths in the cultures described in panel A. Shown are bee swarm plots of the data. The red dot indicates the median, the lines indicate the standard deviation. **(C)** Stability of the indicated mVenus-PbpC variants under phosphate starvation. The indicated strains were cultivated for 24 h in phosphate-limited medium in the absence (uninduced) or presence (induced) of 0.3% xylose and subjected to immunoblot analysis with an anti-GFP antibody. The positions of mVenus-PbpC and free mVenus are indicated on the right.

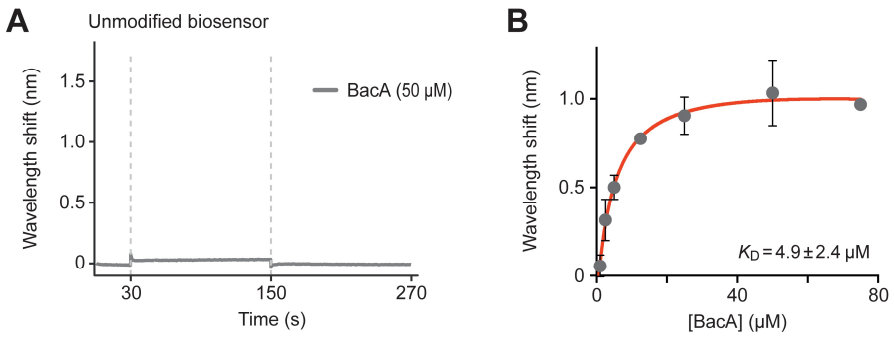

Figure 8–figure supplement 5. Biolayer interferometry analysis of the interaction between PbpC$_{aa1-13}$ and BacA. (A) Control showing the interaction of wild-type BacA (50 µM) with an unmodified biosensor. **(B)** Affinity of BacA for the immobilized PbpC$_{1-13}$ peptide. The final wavelength shifts measured for the different association curves in **Figure 8B** were plotted against the corresponding BacA concentrations. Data represent the average (± SD) of three independent replicates.

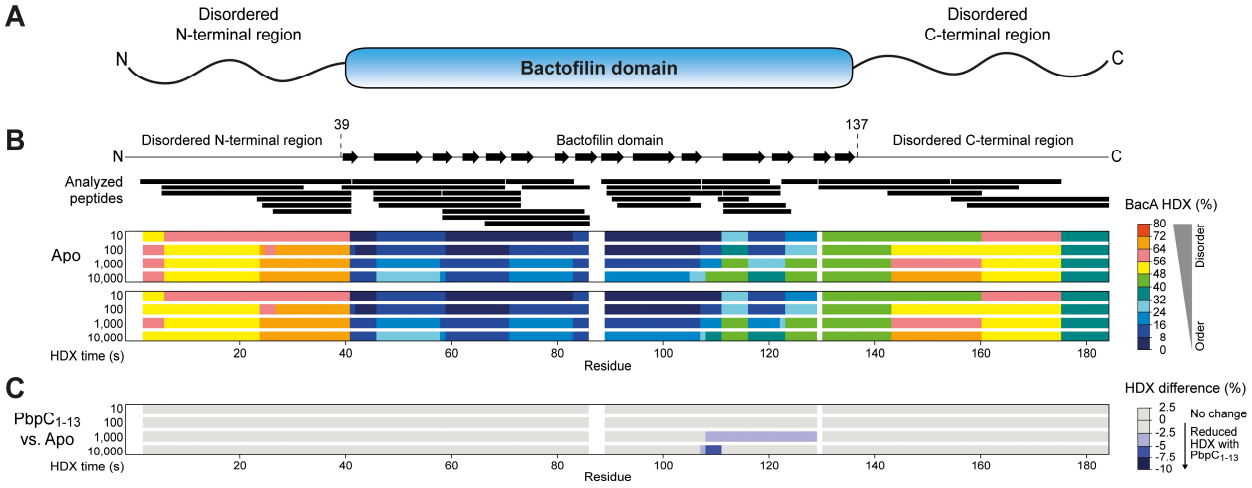

Figure 8–figure supplement 6. Mapping of the PbpC-binding site of BacA by hydrogen-deuterium-exchange (HDX) analysis. (A) Schematic showing the domain structure of BacA. **(B)** HDX analysis of BacA. Purified BacA (2.5 µM) was incubated in deuterated buffer for the indicated time intervals either alone (Apo) or in the presence of PbpC$_{1-13}$ peptide (10 µM). Shown is the degree of HDX along the primary sequence of BacA in the indicated conditions. The color scale is given on the right. The schematic at the top displays the predicted secondary structure of BacA. The black bars represent peptides of BacA that were analyzed for HDX. Residue-specific HDX information was obtained from these overlapping peptides by using the shortest peptide covering a given residue. Gaps indicate amino acid sequences not covered by any peptide. **(C)** HDX difference map. Shown are the residue-specific differences in HDX between BacA in the presence of PbpC$_{1-13}$ peptide and BacA alone that were obtained after the indicated incubation times. The data are projected onto the primary sequence of BacA. The color code is given on the right. Blue color denotes regions showing reduced HDX in the presence of PbpC$_{1-13}$.

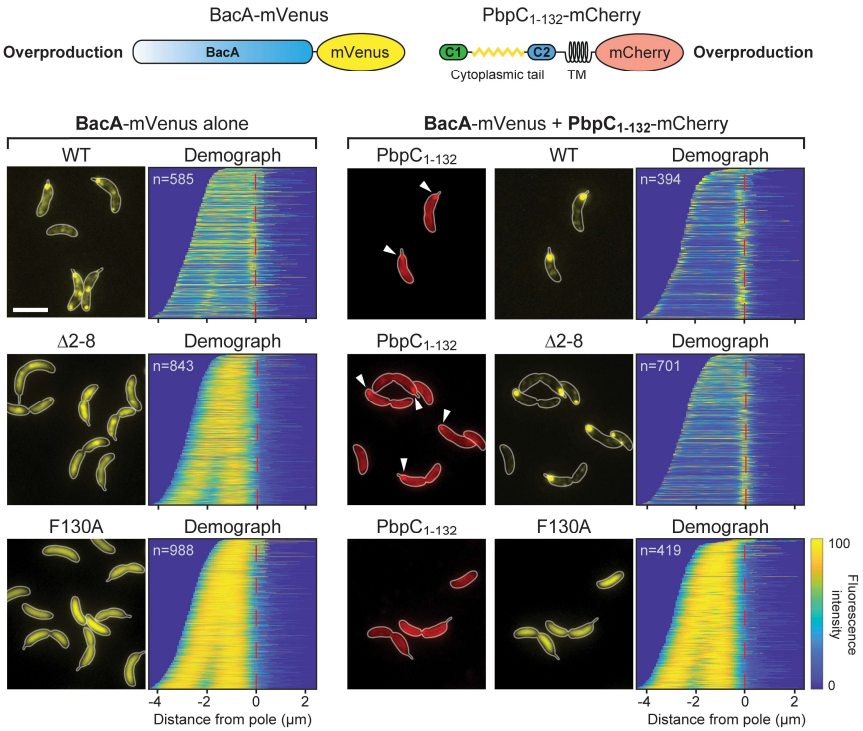

Figure 9. Contribution of PbpC to BacA membrane association. *C. crescentus* Δ*bacAB* Δ*pbpC* cells producing the indicated BacA-mVenus variants (WT, Δ2-8, F130R) under the control of a xylose-inducible promoter and $PbpC_{1-132}$-mCherry under the control of a vanillate-inducible promoter (strains MAB575, MAB576 and MAB577) were grown in the presence of xylose (left) or both xylose and vanillate (right) prior to microscopic analysis. The images show representative fluorescence micrographs, with the cell outlines indicated in white. Arrowheads indicate polar $PbpC_{1-132}$-mCherry foci. Demographs summarizing the single-cell BacA-mVenus fluorescence profiles obtained from random subpopulations of cells are provided next to the respective fluorescence images. The number of cells analyzed is shown in the top left-hand corner of each graph. The schematics on top illustrate the protein constructs used for the analysis (not to scale). Bar: 3 µm.

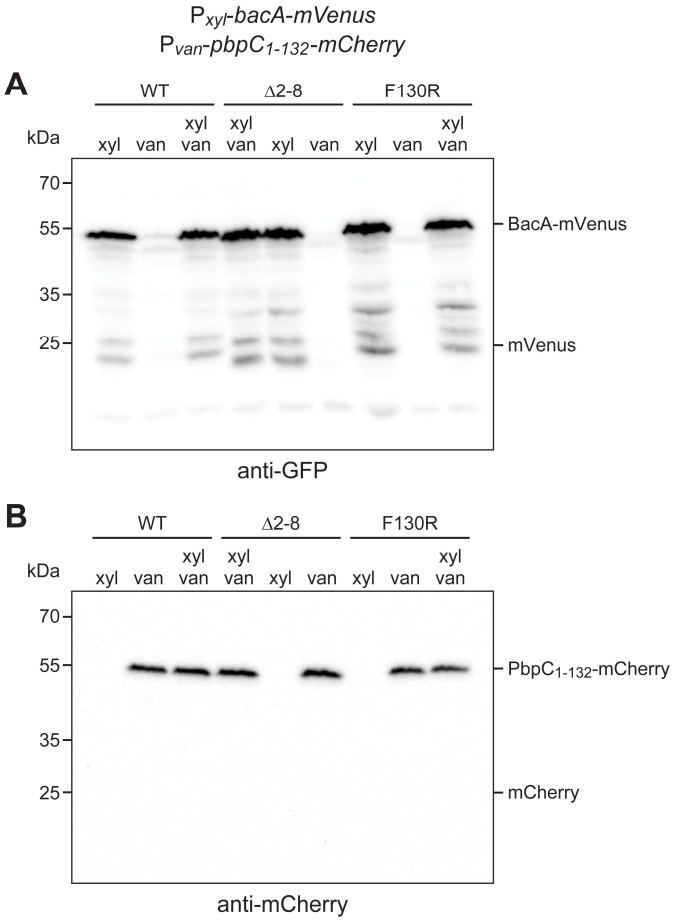

Figure 9–figure supplement 1. Levels and stability the fluorescent fusion proteins used in colocalization studies. *C. crescentus* Δ*bacAB* Δ*pbpC* cells producing the indicated BacA-mVenus variants under the control of a xylose-inducible promoter and $PbpC_{1-132}$-mCherry under the control of a vanillate-inducible promoter (strains MAB575, MAB576 and MAB577) were grown in the presence of xylose (xyl) and/or vanillate (van) and subjected to immunoblot analysis with anti-GFP and anti-mCherry antibodies. The cells analyzed were from the same cultures as those in **Figure 9**. The positions of the fusion proteins and of the corresponding free fluorescent proteins are shown on the right.